University of Crete

Physics Department

&

Foundation of Research and Technology - Hellas (FORTH)

IESL – Photonic Materials and Devices Laboratory

Master Thesis

Study of polypropylene microcavities using whispering gallery mode resonation

Polyxeni Giouni

Supervisor: Dr. Stavros Pissadakis

Heraklion, Crete

2024

Abstract

Whispering gallery modes (WGMs) exhibit unique characteristics, involving high Q factor and sensitivity to refractive index changes. These parameters provide useful information about the material's physical parameters, such as its dimensions, or its mechanical properties under the application of axial strain. The latter, reflects the basis of our experimental work, where light confinement within polypropylene cylindrical microresonators is extensively examined. The main purpose of our experiments is the investigation of WGM spectral behavior under the material's mechanical deformation, in order to determine the photo – elastic properties of polypropylene.

Whispering gallery mode resonances are studied for the first time in polypropylene cylindrically symmetric microcavities. Spectra for both TE and TM polarization states are obtained. Spectral shifts under applied strain are used for determining the strain optical coefficient of polypropylene.

Light propagation and mode formation inside polypropylene resonators is also simulated, with the aid of proper computational programs, in order to estimate the modal eigenstates. These are characterized based on their modal indices and selected WGM spectral description. WGM resonance response under the application of mechanical deformation is extensively studied in this work, providing a non – destructive method for the determination of the material's photo - elastic parameters. An insight of polypropylene's photo – elastic properties is considered very important in the field of applied Photonics, yielding in the application of future photonic devices based on polypropylene's characteristics.

Contents:

1. Introduction

This chapter contains a perceptive introduction to the physics and applications of whispering gallery mode resonators as well as, the aim and structure of this thesis.

1.1 Whispering gallery mode resonators

Whispering gallery modes can be defined as closed beams travelling along circular symmetry microresonators, spatially localized by total internal reflection [1], [2]. Light circulation inside microcavities at specific resonant frequencies is significant in a variety of scientific fields, such as photonics, cavity quantum electrodynamics, biosensing and nonlinear optics [3].

Lord Rayleigh originally studied WGMs in St. Paul's cathedral, in London. He observed that sound (whispers) could be heard in any place near the gallery wall, [4] due to the suppression of wave diffraction occurring when waves are reflected from the wall. [5] In 1909, Debye studied light resonances in dielectric and metallic spheres, taking into consideration WGM resonances [2].

Since then, many studies about whispering gallery modes have been developed at sound waves, also at optical and microwave wavelengths. Such resonances have been observed in various systems and geometries, including cylindrical microcavities, liquid droplets with micrometric – sized volumes, as well as small glass spheres. [6] Whispering gallery modes exhibit remarkable light resonation properties. These high – finesse cavities enhance light interaction with the optical material through high Q – factors achievable in micron - size cavities. The quality factor is defined as the ratio between the energy stored in the resonator and the power dissipated at a resonant frequency, denoting the efficiency of the cavity in trapping light at a specific wavelength. The high quality factor (up to ~ 10^9 for specific materials and configurations) characterized by small modal volumes, make WGM resonators excellent optical

sensor hosts. Figure 1, demonstrates some examples of microresonator cavities with different geometries [7], [8], [9].

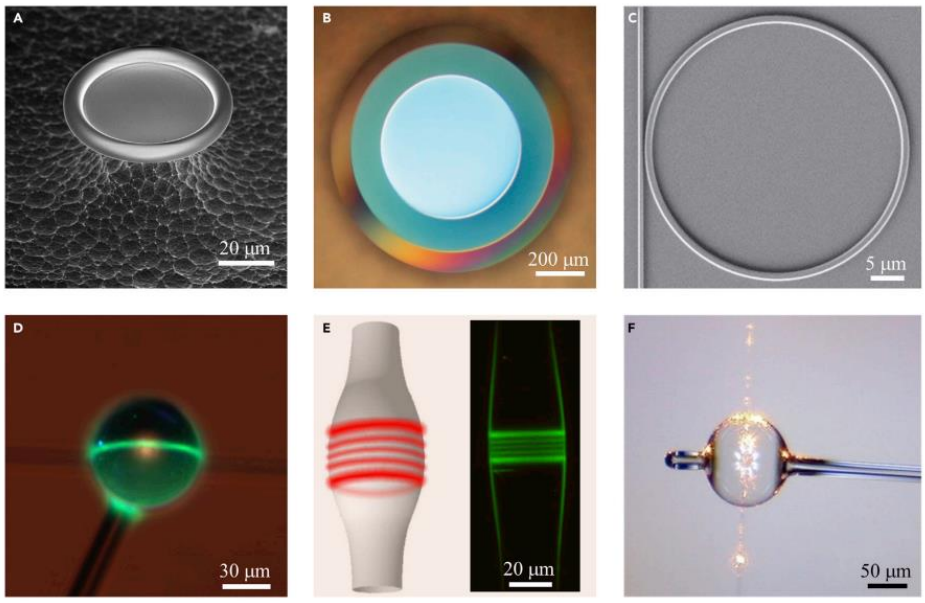

Figure 1: WGM resonator cavities (A) microtoroid (B) microdisk (C) microring (D) microsphere (E) microbottle (F) microbubble [7]

1.2 State of the art on WGM cavities for material characterization

The investigation of a material's photo - elastic properties is a significant approach in correlating macroscopic properties of the material with its micro – coordination structure. Photo – elasticity describes the change in refractivity and birefringence under mechanical stimulation of the optical material under study. In other words photo – elasticity correlates the optical (birefringence) and mechanical (Young's modulus, Poisson's ratio) into a single quantity which in turn reflects the structure of the material in the domain of molar refractivity. Photo – elasticity has been investigated in several experimental configurations (i.e. Twyman – Green interferometry, optical fiber Bragg gratings), while being used for studying structural health state of transparent materials (crack propagation, deformation etc.) [10]. Strain – and stress – optical coefficients of several optical materials have been determined with methods employing whispering gallery mode resonation inside glass and polymeric microcavities,.

Also strain has been used for tuning the resonation properties of polymer and crystalline WGM cavities [11], [45], [46].

Photo – elastic experiments including whispering gallery mode excitation, have been conducted on silk fibroin cylindrical microcavities [12] spherical glassy polymer resonators [11], silica glass, borosilicate fibers and PMMA cylindrical cavities [47], [48], [49]. In all cases, WGM resonances for TE and TM polarization states appear to differentially shift under the application of axial strain, allowing estimation of the strain – induced birefringence and the stress – induced optical coefficient by accounting Young's modulus and Poisson's ratio.

The illustration of the photo – elastic behavior of polymer or glass dielectric materials allows further insights into their segmentation and micro – coordination properties (i.e. poly – dispersity for polymers, or ion – doping for glasses), also helping the development of optical materials and tailored birefringence properties [50].

1.3 Aim of this thesis

The main purpose of this thesis involves the use of whispering gallery mode resonation in polypropylene microcavities for the investigation of the material's photo – elastic properties. There have been extremely few investigations of the photo – elasticity of polypropylene. This is due to the fact that polypropylene is not a widely used optical material since suffers high optical attenuation at visible wavelengths, and high optical scattering behavior due to its poly – crystalline nature (especially for isotactic materials). However, polypropylene has an excellent chemical durability to most inorganic acids/bases and organic solvents, high tensibility and particularly well positioned transparency at THz wavelengths/bands. Polypropylene can also exhibit reversible diffusivity to many organic solvents, rendering that a promising material for the development of chemosensing probes.

In this thesis we couple light inside polypropylene cylindrical cavities (no – core optical waveguides) at the 1550 nm band, and excite/characterize WGMs in those. Then, we apply controlled longitudinal strain onto those polymeric micro

– cavities, measure differential shifts for TE and TM modes and estimate strain – induced birefringence. From those quantities we calculate the strain optical coefficient of polypropylene and by accounting the Young's modulus and Poison's ratio the stress optical coefficient. In addition, we apply powerful simulation tools for identifying modal order in the WGMs excited in those cavities and correlate these findings with the experimental results.

2. Theory

2.1 Light propagation in optical fibers

The main subject of this chapter, is the investigation of light propagation inside optical fibers. Furthermore, the theoretical foundations of waveguide modes are set, employing Maxwell's equations. Finally, the theoretical groundwork of tapered optical fibers is presented.

2.1.1. Optical fibers

Optical fibers are a specific type of waveguides. Optical fibers consist of a core, with refractive index n_1, surrounded by a cladding with refractive index n_0 ($n_1 > n_0$). Light in optical fibers is confined inside the core, as it is supported by total internal reflection. Figure 2, depicts the basic optical fiber structure and its refractive index profile.

The light inside optical fibers is confined forming specific modes. Modes are the solutions of Helmholtz equations for waves. Each mode corresponds to light rays, transmitted at discrete propagation angles, obtained by electromagnetic mode analysis. Modes indicate the way of light propagation in waveguides.

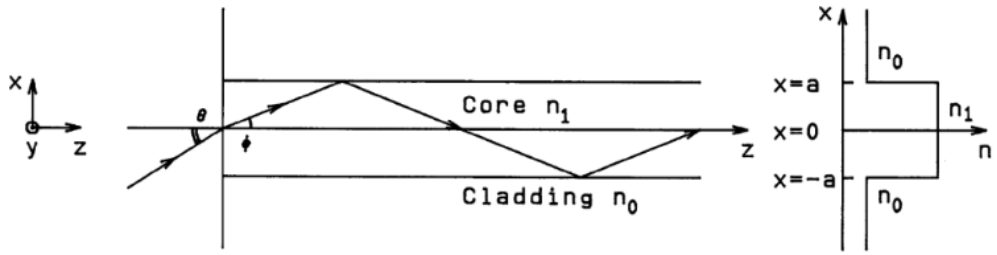

Figure 2: Optical fiber structure and refractive index profile [15]

Two fundamental parameters are commonly used for optical fiber characterization. The first one, is known as the relative core – cladding refractive index difference (Δ) and is defined as [14]:

$$\Delta = \frac{n_1 - n_0}{n_1} \qquad (2.1.1)$$

Furthermore, the normalized frequency (V) is a measure of guidance quality and is defined as:

$$V = k_0 r \sqrt{n_1^2 - n_0^2} \qquad (2.1.2)$$

In Eq. 2.2, $k_0=2\pi/\lambda$, is the wavenumber, with λ being the wavelength and r is the core radius. [15]

Based on the number of modes supported, optical fibers can be divided into two groups: single mode fibers (SMF) and multimode ones. Single mode fibers are designed for allowing the propagation of the same mode, while in multimode fibers, all types of dispersion exist simultaneously. Optical fibers are commonly made of SiO_2. [16, 17] Typical core diameter values in single mode fibers are around 8 μm, with cladding diameter of 125 μm. The core refractive index is 1.447, while the one of the cladding typically equals 1.445. Multimode fibers usually have larger cores than the single mode ones, although the total cladding diameter does not exceed 125 μm. [16]

2.1.2. Total internal reflection

The refraction of electromagnetic waves on the interface between two media of different refractive indices is described by Snell's law [17]:

$$n_1 sin\theta_1 = n_2 sin\theta_2 \qquad (2.1.3)$$

In equation (2.1.3), n_1 and n_2 are the refractive indices between the two media. The angle between the incident wave and the normal vector of the incidence surface is denoted as θ_1. Angle θ_2 is formed between the vector normal to the surface and the refracted wave.

Assuming that light is transmitted from an optically dense to an optically thinner medium ($n_2<n_1$), then refraction occurs when the angle of incidence (θ_1) satisfies the following condition:

$$\theta_1 < \theta_c = sin^{-1}\left(\frac{n_2}{n_1}\right) \qquad (2.1.4)$$

Where, θc is defined as the critical angle. If θ1≥θc, then the incident wave undergoes total internal reflection from the interface separating the two media. In the following paragraph, the electromagnetic field in medium 2 is presented. The electric field in the medium mentioned, can be described as [18], [19]:

$$E_2 = E_{02}e^{i(\boldsymbol{k_2}\cdot\boldsymbol{r}-\omega t)} \qquad (2.1.5)$$

Where,

$$k_2 = \frac{n_2\pi}{\lambda} \qquad (2.1.6)$$

It is $k_2 = k_x+k_y$, where k_x describes the light propagation parallel to the interface and k_y the propagation perpendicular to it. From Snell's law one can obtain:

$$k_x = \left(1 - \frac{n_1^2 sin^2\theta_1}{n_2^2}\right)^{1/2} \qquad (2.1.7)$$

$$k_y = ik_2\left(\frac{n_1^2 sin^2\theta_1}{n_2^2} - 1\right)^{1/2} = i\beta \qquad (2.1.8)$$

Using equation (2.1.7), since k_x is real and k_y is complex, it can be derived:

$$E_2 = E_{02}e^{i(k_x x-\omega t)}e^{-\beta y} \qquad (2.1.9)$$

Equation (2.1.9) describes the evanescent field, which decays exponentially with penetration depth:

$$\frac{1}{\beta} = \frac{\lambda_0}{2\pi\sqrt{n_1^2 sin^2\theta_1 - n_2^2}} \qquad (2.1.10)$$

2.1.3. Waveguide modes in optical fibers

Optical fiber mode analysis is established by Maxwell's equations. These equations, describe the propagation of the electromagnetic fields inside certain materials and structures. In the case of optical fibers specifically, some boundary conditions are also needed for light propagation description. This analysis, starts with the differential form of Maxwell's equations [20], [21]:

$$\boldsymbol{\nabla} \times \boldsymbol{E} = -\frac{\partial \boldsymbol{B}}{\partial t} = -\mu \frac{\partial \boldsymbol{H}}{\partial t} \qquad (2.1.11)$$

$$\boldsymbol{\nabla} \times \boldsymbol{H} = \frac{\partial \boldsymbol{H}}{\partial t} = \varepsilon \frac{\partial \boldsymbol{E}}{\partial t} \qquad (2.1.12)$$

$$\boldsymbol{\nabla} \cdot \boldsymbol{D} = 0 \qquad (2.1.13)$$

$$\boldsymbol{\nabla} \cdot \boldsymbol{B} = 0 \qquad (2.1.14)$$

Where D and H represent the vectors for electric and magnetic displacements and can be defined as:

$$\boldsymbol{D} = \mu \cdot \boldsymbol{E} \qquad (2.1.15)$$

$$\boldsymbol{B} = \mu \cdot \boldsymbol{H} \qquad (2.1.16)$$

We can easily obtain the homogeneous electromagnetic wave equation, as it is written in the two following equations:

$$\left(\boldsymbol{\nabla}^2 - \mu\varepsilon\frac{\partial^2}{\partial t^2}\right)\boldsymbol{E}(r,t) = 0 \qquad (2.1.17)$$

$$\left(\boldsymbol{\nabla}^2 - \mu\varepsilon\frac{\partial^2}{\partial t^2}\right)\boldsymbol{H}(r,t) = 0 \qquad (2.1.18)$$

The solutions of equations (2.1.17) and (2.1.18), for the electric and magnetic field respectively, can be written as:

$$\boldsymbol{E}(r,t) = \boldsymbol{E}(r,\varphi)e^{i(\omega t-\beta z)} \qquad (2.1.19)$$

$$\boldsymbol{H}(r,t) = \boldsymbol{H}(r,\varphi)e^{i(\omega t-\beta z)} \qquad (2.1.20)$$

In general, dielectric waveguides can support a finite number of modes. Optical fibers constitute cylindrical waveguides. Thus, the modal analysis inside them should start with the time – independent wave equation written in the cylindrical coordinate system, (r, φ, z) shown in equations (2.1.21) and (2.1.22).

$$\left[\frac{\partial^2}{\partial r^2} + \frac{1}{r}\frac{\partial}{\partial r} + \frac{1}{r^2}\frac{\partial^2}{\partial \varphi^2} + (k^2 - \beta^2)\right]\boldsymbol{E}(r,\varphi) \qquad (2.1.21)$$

$$\left[\frac{\partial^2}{\partial r^2} + \frac{1}{r}\frac{\partial}{\partial r} + \frac{1}{r^2}\frac{\partial^2}{\partial \varphi^2} + (k^2 - \beta^2)\right]\boldsymbol{H}(r,\varphi) \qquad (2.1.22)$$

Optical fibers are symmetrical structures. Therefore, the homogeneous wave equations can be solved for their r and φ components separately. Since such resonators are cylindrical, we should solve Maxwell's equations in the cylindrical coordinate system. These equations are written below:

$$i\omega\varepsilon E_r = i\beta H_\varphi + \frac{1}{r}\frac{\partial H_z}{\partial \varphi} \qquad (2.1.23)$$

$$i\omega\varepsilon E_\varphi = -i\beta H_r + \frac{\partial H_z}{\partial r} \qquad (2.1.24)$$

$$-i\omega\mu H_r = i\beta E_\varphi + \frac{1}{r}\frac{\partial E_z}{\partial \varphi} \qquad (2.1.25)$$

$$-i\omega\mu H_\varphi = -i\beta E_r - \frac{\partial E_z}{\partial r} \qquad (2.1.26)$$

From equations (2.1.27) to (2.1.30), one can obtain the electric and magnetic field components in cylindrical coordinates, as presented in the following equations:

$$E_r = \frac{-i\beta}{k^2 - \beta^2}\left(\frac{\partial E_z}{\partial r} - \frac{\omega\mu}{\beta}\frac{1}{r}\frac{\partial H_z}{\partial \varphi}\right) \qquad (2.1.27)$$

$$E_\varphi = \frac{-i\beta}{k^2 - \beta^2}\left(\frac{1}{r}\frac{\partial E_z}{\partial \varphi} - \frac{\omega\mu}{\beta}\frac{\partial H_z}{\partial r}\right) \qquad (2.1.28)$$

$$H_r = \frac{-i\beta}{k^2 - \beta^2}\left(\frac{\partial H_z}{\partial r} - \frac{\omega\varepsilon}{\beta}\frac{1}{r}\frac{\partial E_z}{\partial \varphi}\right) \qquad (2.1.29)$$

$$H_\varphi = \frac{-i\beta}{k^2 - \beta^2}\left(\frac{1}{r}\frac{\partial H_z}{\partial \varphi} + \frac{\omega\varepsilon}{\beta}\frac{\partial E_z}{\partial r}\right) \qquad (2.1.30)$$

Now, based on the previous conclusions, we can re – write the time independent wave equation described in equations (2.1.21) and (2.1.22), in cylindrical coordinates as follows:

$$\left[\frac{\partial^2}{\partial r^2} + \frac{1}{r}\frac{\partial}{\partial r}\frac{1}{r^2}\frac{\partial^2}{\partial \varphi^2} + (k^2 - \beta^2)\right]\begin{bmatrix} E_z \\ H_z \end{bmatrix} = 0 \qquad (2.1.31)$$

Where, E_z and H_z are the longitudinal components of the electric and magnetic fields respectively. These components represent the guided modes in optical fibers. By applying the separation of variable method, the mentioned components can be written as solutions of the differential equations (2.1.21) and (2.1.22) as [20]:

$$E_z(r,\varphi) = AR(r)\Phi(\varphi) \;\Rightarrow\; E_z(r,\varphi) = R(r)e^{\pm il\varphi} \quad (2.1.32)$$

$$H_z(r,\varphi) = AR(r)\Phi(\varphi) \;\Rightarrow\; H_z(r,\varphi) = R(r)e^{\pm il\varphi} \quad (2.1.33)$$

Where we assumed the angular function $\Phi(\varphi)$ to have the form $\Phi(\varphi)=Ae^{\pm il\varphi}$, with l being an integer with values l=0,1,2,... Therefore, from equations (2.1.21), (2.1.22), (2.1.32) and (2.1.33), we can derive Bessel's differential equation, for electromagnetic wave propagation in cylindrical structures [20].

$$\frac{\partial^2}{\partial r^2} + \frac{1}{r}\frac{\partial}{\partial r} + \left(k^2 - \beta^2 - \frac{l^2}{r^2}\right)R(r) = 0 \quad (2.1.34)$$

Bessel's function solution is written as:

$$R(r) = \begin{cases} C_1 J_l(hr), & h^2 = k^2 - \beta^2 > 0 \\ C_2 K_l(hr), & -q^2 = k^2 - \beta^2 < 0 \end{cases} \quad (2.1.35)$$

Where $J_l(r)$ and $K_l(r)$ are Bessel's functions of the first and second kind respectively. $J_l(r)$ functions indicate that the electromagnetic field in the center of the optical fiber (r=0) should be finite. At the same time, electromagnetic field components in the fiber cladding exhibit an exponential decay, thus $K_l(r)$ functions are appropriate for their description. In conclusion, the electric and magnetic field longitudinal components inside and outside of the fiber can be written in the following form:

$$\begin{cases} E_z(r,\varphi) = AJ_l(hr)e^{il\varphi} \\ H_z(r,\varphi) = BJ_l(hr)e^{il\varphi} \end{cases}, \qquad r < a \qquad (2.1.36)$$

$$\begin{cases} E_z(r,\varphi) = CK_l(hr)e^{-il\varphi} \\ H_z(r,\varphi) = DK_l(hr)e^{-il\varphi} \end{cases}, \qquad r > a \qquad (2.1.37)$$

Assuming a fiber with radius r=α. A, B, C and D are constants which can be determined with the application of proper boundary conditions. The transverse field components, already mentioned in equations (2.1.27) to (2.1.30) can be written by substituting equations (2.1.36) and (2.1.37) into them.

$$E_r(\boldsymbol{r},t) = \begin{cases} -i\frac{\beta}{h^2}\left[AhJ_l'(hr) + i\frac{\omega\mu l}{\beta r}BJ_l(hr)\right], r < a \\ i\frac{\beta}{q^2}\left[CqK_l'(qr) + i\frac{\omega\mu l}{\beta r}DK_l(qr)\right], r > a \end{cases} \times e^{il\varphi}e^{i(\omega t-\beta z)} \qquad (2.1.38)$$

$$E_\varphi(\boldsymbol{r},t) = \begin{cases} -i\frac{\beta}{h^2}\left[\frac{il}{r}AhJ_l(hr) - i\frac{\omega\mu}{\beta}BJ_l'(hr)\right], r < a \\ i\frac{\beta}{q^2}\left[\frac{il}{r}CqK_l(qr) - i\frac{\omega\mu}{\beta r}DqK_l'(qr)\right], r > a \end{cases} \times e^{il\varphi}e^{i(\omega t-\beta z)} \qquad (2.1.39)$$

$$H_r(\boldsymbol{r},t) = \begin{cases} -i\frac{\beta}{h^2}\left[BhJ_l'(hr) + i\frac{\omega\varepsilon_1 l}{\beta r}AJ_l(hr)\right], r < a \\ i\frac{\beta}{q^2}\left[DqK_l'(qr) + i\frac{\omega\varepsilon_2 l}{\beta r}CK_l(qr)\right], r > a \end{cases} \times e^{il\varphi}e^{i(\omega t-\beta z)} \qquad (2.1.40)$$

$$H_\varphi(\boldsymbol{r},t) = \begin{cases} -i\frac{\beta}{h^2}\left[\frac{il}{r}BhJ_l(hr) - i\frac{\omega\varepsilon_1}{\beta}AJ_l'(hr)\right], r < a \\ i\frac{\beta}{q^2}\left[\frac{il}{r}DK_l(qr) - i\frac{\omega\varepsilon_2}{\beta r}CqK_l'(qr)\right], r > a \end{cases} \times e^{il\varphi}e^{i(\omega t-\beta z)} \qquad (2.1.41)$$

In order to obtain the constants A, B, C and D included in the field components, the continuity equation of both the electric and magnetic field should be solved at the interface separating the core from the cladding (r=α):

$$J_l(ha)A - K_l(qa)C = 0 \qquad (2.1.42)$$

$$\left[\frac{il}{h^2a}J_l(ha)\right]A+\left[-\frac{\omega\mu}{h\beta}J_l'(ha)\right]B+\left[\frac{il}{q^2a}K_l(qa)\right]C+\left[-\frac{\omega\mu}{h\beta}J_l'(ha)\right]D=0 \quad (2.1.43)$$

$$J_l(ha)B-K_l(qa)D=0 \qquad (2.1.43)$$

$$\left[\frac{\omega\varepsilon_1}{h^2\beta}J_l'(ha)\right]A+\left[\frac{il}{h^2a}J_l(ha)\right]B+\left[\frac{\omega\varepsilon_2}{q\beta}K_l'(qa)\right]C+\left[\frac{il}{q^2a}K_l(qa)\right]D=0 \quad (2.1.44)$$

After solving the equations (2.1.42) up to (2.1.44), we obtain the time – dependent solutions of electromagnetic fields longitudinal components as:

$$E_z(\boldsymbol{r},t)=\begin{cases}AJ_l(hr)e^{il\varphi}e^{i(\omega t-\beta z)}, & r<a\\ CK_l(hr)e^{il\varphi}e^{i(\omega t-\beta z)}, & r>a\end{cases} \quad (2.1.45)$$

$$H_z(\boldsymbol{r},t)=\begin{cases}BJ_l(hr)e^{il\varphi}e^{i(\omega t-\beta z)}, & r<a\\ DK_l(hr)e^{il\varphi}e^{i(\omega t-\beta z)}, & r>a\end{cases} \quad (2.1.46)$$

Transverse electric (TE) modes correspond to E_z=0 and E_φ, H_r, $H_z \neq 0$. Similarly, transverse magnetic (TM) modes correspond to H_z=0 and E_r, E_z, $H_\varphi \neq 0$. The electric field vectors and intensity profile correlation is depicted in Figure 3 below.

LP mode Designations	Traditional mode Designations	Electric filed Distribution	Intensity Distribution of E_z
$LP_{11}\begin{cases} l=0 \\ m=1 \end{cases}$	$HE_{11}\begin{cases} l=0 \\ m=1 \end{cases}$		
$LP_{01}\begin{cases} l=1 \\ m=1 \end{cases}$	$\begin{cases} TE_{01}\begin{cases} l=0 \\ m=1 \end{cases} \\ TM_{01}\begin{cases} l=0 \\ m=1 \end{cases} \\ HE_{21}\begin{cases} l=1 \\ m=1 \end{cases} \end{cases}$		
$LP_{21}\begin{cases} l=2 \\ m=1 \end{cases}$	$\begin{cases} HE_{11}\begin{cases} l=2 \\ m=1 \end{cases} \\ HE_{21}\begin{cases} l=2 \\ m=1 \end{cases} \end{cases}$	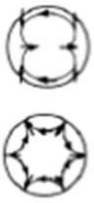	

Figure 3: Electric field vectors and intensity profiles of the three first modes [22]

2.1.4. Tapered optical fibers

As mentioned earlier, the normalized frequency (V) is a measure of the guidance quality of a waveguide. Thus, this quantity provides information about higher order mode transmission. A specific kind of optical fiber structures, allowing the transmission of specific order modes which interact well with the outer environment are optical fiber tapers (OFTs). These structures are specially thinned optical fibers, where modes propagate in the cladding at a specific point. OFT fabrication includes heating of a single mode optical fiber, leading to melting and softening of the material, while, the fiber undergoes a tensile force. [23]

The structure of an optical fiber taper includes an untapered region, a region corresponding to taper transition and the taper waist region, with the smallest diameter, achieved after material melting. Tapering of the optical fiber leads to a modal field distribution shift. The diameter change rate of the taper, results in a variation in energy transfer from the fundamental mode to the closest higher order modes. [23], [24]

An optical fiber taper is considered adiabatic when the initial fundamental fiber mode is converted to a fundamental mode inside the taper. This condition occurs when there is minimum power coupling between the core and cladding modes, and scattering losses are minimized as well, during light propagation inside the tapered region. [25] In adiabatic tapers, the beat length between the fundamental mode and the one of the first higher order mode (z_b), is connected with the local taper length (z_t) as:

$$z_b < z_t \qquad (2.1.47)$$

$$z_b = \frac{2\pi}{\beta_1 - \beta_2} \qquad (2.1.48)$$

$$z_t = \frac{\rho}{tan\Omega} \quad (2.1.49)$$

In the above equations, $\beta_1(r)$ and $\beta_2(r)$ correspond to the propagation constants of fundamental and second order mode at radius r respectively. $\rho=\rho(z)$ refers to the radius of the local core, and $\Omega=\Omega(z)$ is the taper angle. Therefore,

$$\left|\frac{\partial\rho}{\partial z}\right| = tan\Omega < \frac{\rho(\beta_1 - \beta_2)}{2\pi} \qquad (2.1.50)$$

With $\left|\frac{\partial\rho}{\partial z}\right|$ defined as the rate of change in the radius of the local core, leading to:

$$\left|\frac{\partial r}{\partial z}\right| < \frac{r(\beta_1 - \beta_2)}{2\pi} \qquad (2.1.51)$$

Therefore, according to the conditions mentioned above, the fiber radius should decrease gradually in order to prevent the excitation of higher order modes. [24]

2.2. Whispering gallery mode theory

2.2.1. Whispering gallery modes

Whispering gallery modes (WGMs) are extensively investigated in this thesis. In such resonators, light propagates along a circular path where it is confined by total internal reflection, leading to modal formation with high quality factors and small volumes. The geometry and composition of a WGM microresonator strongly affects many resonant parameters, including the resonant frequencies observed, and the modal quality factors. [26]

In order to investigate various WGM resonator applications, some spectral parameters need to be taken into account, starting with the modal power, which distribution is defined by a Lorentzian function [27]:

$$P(\omega) = P_0 \frac{\frac{\gamma_0^2}{2}}{(\omega - \omega_0)^2 + \frac{\gamma_0^2}{2}} \qquad (2.2.1)$$

Where, ω_o is the resonant frequency, γ_o defines the full width at half maximum (FWHM) of this distribution, and P_o refers to the power amplitude. The resonant wavelength λ_o and the FWHM, also expressed as $\Delta\lambda$, are related to the quality factor (Q – factor) of the resonance as [28]:

$$Q = \frac{\lambda_0}{\Delta\lambda} \qquad (2.2.2)$$

The total resonance linewidth is highly affected by loss mechanisms, including radiation, light scattering at resonator surface, bulk scattering and light absorption from the material. Therefore, the WGM resonance FWHM can be written as $\Delta\lambda = \Delta\lambda_{rad} + \Delta\lambda_{sca} + \Delta\lambda_{mat} + \ldots$, while Q factor is influenced as $Q^{-1} = Q_{rad}^{-1} + Q_{sca}^{-1} + Q_{mat}^{-1} + \ldots$. Losses attributed to radiation are dominant in smaller resonators, while absorption becomes the main loss mechanism as the cavity size is increased. [29], [30], [31]

2.2.2. Wave equation in cylindrical resonators

WGM propagation is azimuthal in resonators with rotational symmetry, including cylindrical resonators. The resonances occur at specific wavelengths, with their spectral positions being directly dependent on the resonator radius and refractive index. WGMs inside microresonators are supported by total internal reflection, leading to a continuous wave propagation along the microresonator's surface. The condition in which resonances occur relates the resonant wavelengths with the radius and refractive index by the following equation:

$$\lambda_R = \frac{2\pi\alpha n_{eff}}{m} \qquad (2.2.3)$$

Where, λ_R refers to the wavelengths in which resonances occur, n_{eff} is the WGM effective index, α is the microresonator's radius and m is the azimuthal modal order, corresponding to the total number of wavelengths around the microresonator.

In the case of cylindrical microresonators, n_{eff}, are obtained from the solutions of Maxwell's equations combined with the proper boundary conditions. Cylindrical resonators have translational symmetry around axial direction, where two regions with different refractive indices can be defined as: region I, with refractive index n_1 and region II with refractive index n_2, with $n_1 > n_2$. In general, there is a difference in the material's refractive index (n_1) in the axial and transversal directions, mentioned as n_{1z} and n_{1t} respectively. According to the above, a refractive index tensor can be defined as [32]:

$$n_2 = \begin{pmatrix} n_{1t} & 0 & 0 \\ 0 & n_{1t} & 0 \\ 0 & n_{1z} & 0 \end{pmatrix} \qquad (2.2.4)$$

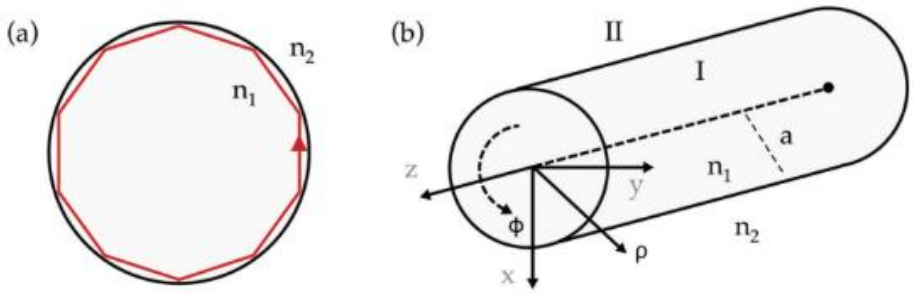

Figure 4: (a) WGM azimuthal propagation inside a microresonator (b) Cylindrical coordinate system with mentioned regions [32]

In this case, region I is assumed to be a dielectric medium with anisotropic permittivity $\varepsilon_0\varepsilon_1$, while region II, is assumed to be an infinite dielectric medium (typically air) with isotropic permittivity $\varepsilon_0\varepsilon_2$. Both regions have the same magnetic permeability μ_0.

Since wave propagation in cylindrical resonators is entirely azimuthal, the electric and magnetic field components depend on the parameter $e^{-i\beta\varphi}$, with β being the propagation constant. Also, the electromagnetic field exhibits a harmonic time dependence described as $e^{j\omega t}$. Therefore, the electric and magnetic field vectors, obtained from Maxwell's equations solutions in cylindrical coordinates, can be written as:

$$\boldsymbol{E}(\boldsymbol{r},t) = \boldsymbol{e}(\rho)e^{-i\beta\varphi}e^{j\omega t} \qquad (2.2.5\ \alpha)$$

$$\boldsymbol{H}(\boldsymbol{r},t) = \boldsymbol{h}(\rho)e^{-i\beta\varphi}e^{j\omega t} \qquad (2.2.5\ b)$$

With electromagnetic field amplitudes described as:

$$\boldsymbol{e}(\rho) = e_\rho(\rho)\widehat{\boldsymbol{u}_\rho} + e_\varphi(\rho)\widehat{\boldsymbol{u}_\varphi} + e_z(\rho)\widehat{\boldsymbol{u}_z} \qquad (2.2.6\ a)$$

$$\boldsymbol{h}(\rho) = h_\rho(\rho)\widehat{\boldsymbol{u}_\rho} + h_\varphi(\rho)\widehat{\boldsymbol{u}_\varphi} + h_z(\rho)\widehat{\boldsymbol{u}_z} \qquad (2.2.6\ b)$$

The amplitude of both the electric and magnetic fields depends entirely on the radial coordinate (r) and not on z, since the cylinder length is assumed to be infinite. Translational direction is also assumed to be symmetrical. The anisotropy tensor of the material can be descried as:

$$\bar{\varepsilon} = \begin{pmatrix} \varepsilon_t & & \\ & \varepsilon_t & \\ & & \varepsilon_z \end{pmatrix} \qquad (2.2.7)$$

With ε_t being the anisotropy component transversal to z coordinate and ε_z being parallel to z coordinate.
According to the above, Maxwell's equations can be written as:

$$\nabla \times (\nabla \times \boldsymbol{E}) = \omega^2 \mu_0 \varepsilon_0 \bar{\varepsilon} \boldsymbol{E} \qquad (2.2.8\ \alpha)$$

$$\nabla \times (\bar{\varepsilon}^{-1} \nabla \times \boldsymbol{H}) = \omega^2 \mu_0 \varepsilon_0 \boldsymbol{H} \qquad (2.2.8\ b)$$

The wave equations describing the axial components are:

$$\left[\rho^2 \partial_\rho^2 + \rho \partial_\rho + \left(\rho^2 k_0^2 \varepsilon_z - \beta_\varphi\right)\right] \varepsilon_z(\rho) = 0 \qquad (2.2.9\ \alpha)$$

$$\left[\rho^2 \partial_\rho^2 + \rho \partial_\rho + \left(\rho^2 k_0^2 \varepsilon_t - \beta_\varphi\right)\right] h_z(\rho) = 0 \qquad (2.2.9\ b)$$

In the above equations, k_o is denoted as the vacuum wavenumber. The form of equations (2.2.9 a) and (2.2.9 b) resembles the one of Bessel's equation. Boundary conditions need to be applied at the interface between the different regions. WGM resonant waves propagate azimuthally, leading to their self – confinement after each round trip on the resonator's surface. Therefore, the confined wave phase should have a difference of 2π to the previous one, after each round trip is completed. The modes supported by a microresonator, can be divided into three groups, depending on their polarization: hybrid modes, TE modes and TM modes. [20] Hybrid modes propagating entirely azimuthally

cannot exist in the case of dielectric isotropic cylindrical resonators.[33] Therefore, the electromagnetic field components for each region in cylindrical coordinates, for both TE and TM polarization states can be described as:

TM Modes:

Region I (ρ<α):

$$E_z^I = A_1 J_m(k_0 n_{1z}\rho)e^{-jm\varphi}e^{i\omega t}$$

$$H_\rho^I = \frac{m}{\omega\mu_0}\frac{1}{\rho}A_1 J_m(k_0 n_{1z}\rho)e^{-jm\varphi}e^{i\omega t}$$

$$H_\varphi^I = \frac{k_0 n_{1z}}{j\omega\mu_0}A_1 J_m'(k_0 n_{1z}\rho)e^{-jm\varphi}e^{i\omega t} \qquad (2.2.10)$$

$$E_\rho^I = E_\varphi^I = H_z^I = 0$$

Region II (ρ>α):

$$E_z^{II} = A_2 H_m^{(2)}(k_0 n_2\rho)e^{-jm\varphi}e^{i\omega t}$$

$$H_\rho^{II} = \frac{m}{\omega\mu_0}\frac{1}{\rho}A_2 H_m^{(2)}(k_0 n_2\rho)e^{-jm\varphi}e^{i\omega t}$$

$$H_\varphi^{II} = \frac{k_0 n_2}{j\omega\mu_0}A_2 H_m^{(2)\prime}e^{-jm\varphi}e^{i\omega t} \qquad (2.2.11)$$

$$E_\rho^{II} = E_\varphi^{II} = H_z^{II} = 0$$

TE Modes:

Region I (ρ<α):

$$H_z^I = B_1 J_m(k_0 n_{1t}\rho)e^{-jm\varphi}e^{i\omega t}$$

$$E_\rho^I = -\frac{m}{\omega\varepsilon_0\varepsilon_t}\frac{1}{\rho}B_1 J_m(k_0 n_{1t}\rho)e^{-jm\varphi}e^{i\omega t}$$

$$E_\varphi^I = -\frac{k_0 n_{1t}}{j\omega\mu_0}B_1 J_m'(k_0 n_{1z}\rho)e^{-jm\varphi}e^{i\omega t} \qquad (2.2.12)$$

$$H_\rho^I = H_\varphi^I = E_z^I = 0$$

Region II (ρ>α):

$$H_z^{II} = B_2 H_m^{(2)}(k_0 n_2\rho)e^{-jm\varphi}e^{i\omega t}$$

$$E_\rho^{II} = -\frac{m}{\omega\varepsilon_0\varepsilon_2}\frac{1}{\rho}B_2 H_m^{(2)}(k_0 n_2\rho)e^{-jm\varphi}e^{i\omega t}$$

$$E_\varphi^{II} = -\frac{k_0 n_2}{j\omega\varepsilon_0\varepsilon_2}B_1 H_m^{(2)'}(k_0 n_2\rho)e^{-jm\varphi}e^{i\omega t} \qquad (2.2.13)$$

$$H_\rho^{II} = H_\varphi^{II} = E_z^{II} = 0$$

In the above equations, J_m represents the Bessel function of the first kind, while H_m is Hankel function of second kind. Boundary conditions on the interface between the different regions (ρ=α) can be written as:

TM Modes:

$$E_z^I(\rho=\alpha) = E_z^{II}(\rho=\alpha)$$
$$H_\varphi^I(\rho=\alpha) = H_\varphi^{II}(\rho=\alpha) \qquad (2.2.14\ a)$$

TE Modes:

$$H_z^I(\rho=\alpha) = H_z^{II}(\rho=\alpha)$$
$$E_\varphi^I(\rho=\alpha) = E_\varphi^{II}(\rho=\alpha) \qquad (2.2.14\ b)$$

The application of the above boundary conditions leads to the generation of TM and TE modes characteristic equations respectively [20], [32]:

$$n_{1z}\frac{J_m'(k_0 n_{1z}\alpha)}{J_m(k_0 n_{1z}\alpha)} = n_2\frac{H_m^{(2)\prime}(k_0 n_2\alpha)}{H_m^{(2)}(k_0 n_2\alpha)}\ (TM) \qquad (2.2.15\ a)$$

$$\frac{1}{n_t}\frac{J_m'(k_0 n_{1z}\alpha)}{J_m(k_0 n_{1z}\alpha)} = \frac{1}{n_2}\frac{H_m^{(2)\prime}(k_0 n_2\alpha)}{H_m^{(2)}(k_0 n_2\alpha)}\ (TE) \qquad (2.2.15\ b)$$

2.2.3. Tapered optical fiber – resonator coupling

In order to observe high Q factor whispering gallery modes, it is crucial to achieve an efficient coupling between the optical fiber taper and the microresonator. This section includes a theoretical approach related to energy coupling into the examined resonator. In the system, there is an input electric field, denoted as E_i, which is responsible for the coupling between the taper and the microresonator. Part of this input field is reflected back (E_r), while another part exerts the optical fiber taper and does not contribute to the coupling process (E_t). Parameter η refers to the coupling strength between the taper and the resonator under investigation. Its value indicates the overlapping degree

between fiber and microresonator fields. The value of g constant indicates the coupling coefficient between two counter – propagating fields (E_{cw} and E_{ccw}) due to in homogeneities on the surface between the fiber and the resonator.

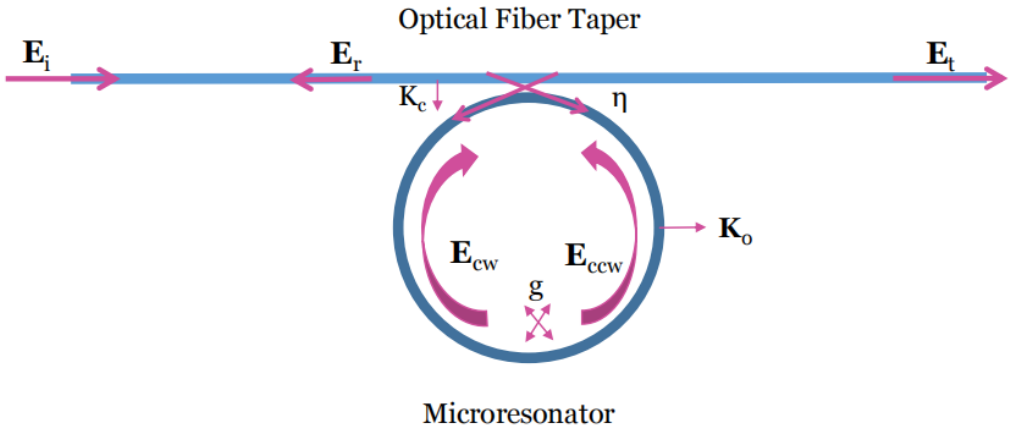

Figure 5: Schematic description of field coupling between an optical fiber taper and a microresonator

Meanwhile, Kc describes the coupling rate and is defined as [34]:

$$K_c = \frac{\eta^2}{2\tau} = \frac{\omega}{2Q_c} \qquad (2.2.16)$$

The equations describing coupling mode are:

$$E_{ccw}(t) = j\eta E_i(t) + \sqrt{1-\eta^2}E_{ccw}(t-\tau)e^{-k_0\tau}e^{j\delta\omega\tau} + jg\tau E_{cw}(t)$$

$$E_{cw}(t) = jg\tau E_{ccw}(t) + \sqrt{1-\eta^2}E_{cw}(t-\tau)e^{-k_0\tau}e^{j\delta\omega\tau} \qquad (2.2.17)$$

$$E_r(t) = j\eta E_{cw}(t)$$

$$E_t(t) = j\eta E_{ccw}(t) + \sqrt{1-\eta^2}E_i(t)$$

Assuming that the system has low losses, the above set of equations can be also written as:

$$\frac{d_{ccw}}{dt} = -(k_0 + k_c - j\delta\omega)E_{ccw}(t) + j\frac{\eta}{\tau}E_i + jgE_{cw}(t)$$

$$\frac{d_{cw}}{dt} = -(k_0 + k_c - j\delta\omega)E_{cw}(t) + jgE_{ccw}(t) \qquad (2.2.18)$$

$$E_r(t) = j\eta E_{cw}(t)$$

$$E_t(t) = j\eta E_{ccw}(t) + \sqrt{1-\eta^2}E_i(t)$$

In a stationary system, the transmittance and reflectivity can be defined as:

$$T(\omega) = \left|\frac{E_t}{E_i}\right|^2 = \left|\sqrt{1-\eta^2} - \frac{2k_c(k_0 + k_c - j\delta\omega)}{(k_0 + k_c - j\delta\omega)^2 + g^2}\right|^2$$

$$R(\omega) = \left|\frac{E_r}{E_i}\right|^2 = \left|\frac{2k_c g}{(k_0 + k_c - j\delta\omega)^2 + g^2}\right|^2 \qquad (2.2.19)$$

2.3. Strain – Optical effect in cylinders

The term “strain – optical effect” describes the change in the optical properties of a material under the application of mechanical strain. The relative dielectric permittivity tensor describes this effect in terms of the induced strain and is defined as [35], [36]:

$$\boldsymbol{\eta}_{i,j}(\varepsilon) = \boldsymbol{\eta}_{i,j}^{(0)} + \Delta\boldsymbol{\eta}_{i,j}(\varepsilon) = \boldsymbol{\eta}_{i,j}^{(0)} + \sum_{k,l} \boldsymbol{p}_{i,j,k,l}\boldsymbol{\varepsilon}_{k,l} \qquad (2.3.1)$$

In the above equation, $\boldsymbol{\eta}_{i,j}^{(0)}$ refers to the impermeability tensor of the non – disturbed material, while $\boldsymbol{p}_{i,j,k,l}$ correspond to the strain – optical coefficients.

The strain tensor induces a symmetry ($\boldsymbol{\eta}_{i,j} = \boldsymbol{\eta}_{j,i}$) a simpler equation for the relative permittivity tensor can be written using the notation of m and n indices as:

$$\boldsymbol{\eta}_m(\varepsilon) = \boldsymbol{\eta}_m^{(0)} + \Delta\boldsymbol{\eta}_m(\varepsilon) = \boldsymbol{\eta}_m^{(0)} + \sum_{k,l} \boldsymbol{p}_{m,n}\boldsymbol{\varepsilon}_n \qquad (2.3.2)$$

Strain – optical coefficients are dimensionless quantities, forming a tensor, which is written as follows for the case of isotropic materials:

$$\boldsymbol{p}_{i,j} = \begin{pmatrix} p_{11} & p_{12} & p_{12} & \cdots & & & \\ p_{12} & p_{11} & p_{12} & \cdots & & & \\ p_{11} & p_{12} & p_{11} & \cdots & & & \\ \cdots & \cdots & \cdots & \cdots & p_{44} & & \\ \cdots & \cdots & \cdots & \cdots & \cdots & p_{44} & \\ \cdots & \cdots & \cdots & \cdots & \cdots & & p_{44} \end{pmatrix} \qquad (2.3.3)$$

With $p_{44} = \frac{1}{2}(p_{11} - p_{12})$. At this point, it is essential to describe the deformation of a cylinder under the strain application along its axial direction.

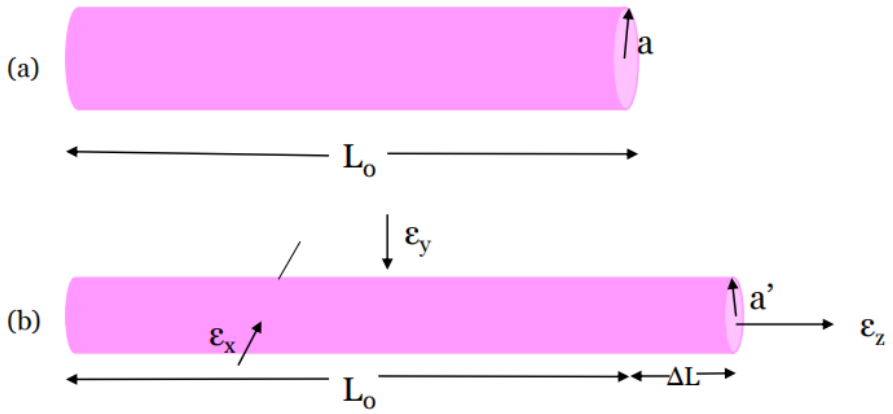

Figure 6: (a) Cylinder of length L_o under equilibrium (b) Cylinder of length L_o under strain application

Under the application of strain, the cylinder with length Lo and radius r in its initial condition, undergoes a deformation due to the strain induced on it. As a

result, its initial length increases to a factor ΔL and its radius decreases from the initial value a to a value a', in the way that is depicted in Figure 6. The axial deformation, noted as ε_z, is responsible for material elongation and equals $\varepsilon_z = \Delta L/L_o$. Except from the elongation, the material also undergoes deformations in its two transversal directions. The ratio between these deformations is described through Poisson's ratio: $v=-\varepsilon_x/\varepsilon_z=-\varepsilon_y/\varepsilon_z$. According to the above, the impermeability variation tensor can be described as:

$$\begin{pmatrix} \Delta\eta_x \\ \Delta\eta_y \\ \Delta\eta_z \\ \Delta\eta_{xy} \\ \Delta\eta_{yz} \\ \Delta\eta_{zy} \end{pmatrix} = \begin{pmatrix} p_{11} & p_{12} & p_{12} & \cdots & & \\ p_{12} & p_{11} & p_{12} & \cdots & & \\ p_{11} & p_{12} & p_{11} & \cdots & & \\ \cdots & \cdots & \cdots & \cdots & p_{44} & \\ \cdots & \cdots & \cdots & \cdots & \cdots & p_{44} \\ \cdots & \cdots & \cdots & \cdots & \cdots & p_{44} \end{pmatrix} \begin{pmatrix} -v\varepsilon_z \\ -v\varepsilon_z \\ \varepsilon_z \\ 0 \\ 0 \\ 0 \end{pmatrix} \qquad (2.3.4)$$

The refractive index of a material is related with the electric and magnetic permittivity (ε_r and μ_r respectively) as $n = \sqrt{\varepsilon_r \mu_r}$, with $\mu_r=1$ at optical frequencies. Therefore, the impermeability variation tensor can also be described through the strain – induced variation tensor as:

$$\begin{pmatrix} \Delta\varepsilon_x^{-1} \\ \Delta\varepsilon_y^{-1} \\ \Delta\varepsilon_z^{-1} \end{pmatrix} = \begin{pmatrix} p_{11} & p_{12} & p_{12} \\ p_{12} & p_{11} & p_{12} \\ p_{12} & p_{12} & p_{11} \end{pmatrix} \begin{pmatrix} -v\varepsilon_z \\ -v\varepsilon_z \\ \varepsilon_z \end{pmatrix} \qquad (2.3.5)$$

The above equation can also be obtained in the form:

$$\Delta n = \frac{1}{(n+\Delta n)^2} - \frac{1}{n^2} = \begin{pmatrix} p_{11} & p_{12} & p_{12} \\ p_{12} & p_{11} & p_{12} \\ p_{12} & p_{12} & p_{11} \end{pmatrix} \begin{pmatrix} -v\varepsilon_z \\ -v\varepsilon_z \\ \varepsilon_z \end{pmatrix} \qquad (2.3.6)$$

Assuming $\frac{\Delta n}{n} \to 0$ and $\frac{\Delta n}{n} = x$, a Taylor series expansion of function $\frac{1}{(1+x^2)}$ around x=0, results in:

$$\begin{pmatrix} \Delta n_x \\ \Delta n_y \\ \Delta n_z \end{pmatrix} = -\frac{n^3}{2}\begin{pmatrix} p_{11} & p_{12} & p_{12} \\ p_{12} & p_{11} & p_{12} \\ p_{12} & p_{12} & p_{11} \end{pmatrix}\begin{pmatrix} -v\varepsilon_z \\ -v\varepsilon_z \\ \varepsilon_z \end{pmatrix} \qquad (2.3.7)$$

The variations of refractive index can be written in terms of longitudinal (Δn_z) and transversal ($\Delta n_x = \Delta n_y = \Delta n_t$) directions respectively as:

$$\Delta n_z = -\frac{n^3}{2}[p_{11} - 2vp_{12}]\varepsilon_z \qquad (2.3.8)$$

$$\Delta n_t = -\frac{n^3}{2}[-vp_{11} + (1-v)p_{12}]\varepsilon_z \qquad (2.3.9)$$

Equations (2.3.8) and (2.3.9) can be rewritten in terms of Pockel's coefficients for TM and TE polarization states respectively as:

$$\frac{\Delta n_z}{n\varepsilon_z} = -\frac{n^2}{2}[p_{11} - 2vp_{12}] = p_{TM} \qquad (2.3.10)$$

$$\frac{\Delta n_t}{n\varepsilon_z} = -\frac{n^2}{2}[-vp_{11} + (1-v)p_{12}] = p_{TE} \qquad (2.3.11)$$

As mentioned earlier, the application of axial strain on a cylindrical resonator results in a change of its radius. This change also affects the resonant positions. These changes in radius and resonant wavelengths are described by the following equations:

$$\Delta\alpha = -\alpha v\varepsilon_z = -av\frac{\Delta L}{L_0} \qquad (2.3.12)$$

$$\frac{\Delta\lambda_R}{\lambda_R} = \left(\frac{1}{a}\frac{da}{dS_z} + \frac{1}{n_{eff}}\frac{dn_{eff}}{dS_z}\right)\Delta\varepsilon_z \qquad (2.3.13)$$

Where, $m\lambda_R=2\pi n_{eff}$. Combining these equations, we can obtain a first – order approximation of the resonant wavelength shifts [37]:

$$\left[\frac{\Delta\lambda_R}{\lambda_R}\right]_{TE,TM} = \frac{\Delta\alpha}{\alpha} + \left(1 - C_{TE,TM}\right)\frac{\Delta n_{t,z}}{n_0} \qquad (2.3.14)$$

With $C_{TE,\,TM}$ being a coefficient related with the resonant wavelength, the microresonator radius and the material's refractive index. The slopes of resonant wavelength shifts as a function of strain for each polarization state, $S_{TE,\,TM}$, can be written as:

$$S_{TE,TM} = -v - \left(1 - C_{TE,TM}\right)p_{et,ez} \qquad (2.3.15)$$

The change in refractive index, phenomenon described as birefringence, is then calculated as:

$$\frac{\Delta n_{strain}}{n_0} = \frac{\Delta n_{TM}}{n_0} - \frac{\Delta n_{TE}}{n_0} = \frac{\Delta\lambda_{TM}}{\lambda_{TM}} - \frac{\Delta\lambda_{TE}}{\lambda_{TE}} \qquad (2.3.16)$$

According to the above, the strain optical coefficient is defined as:

$$K' \equiv \frac{\Delta n_{strain}}{\varepsilon_z(1+v)} = \frac{n^3}{2}(p_{12} - p_{11}) \qquad (2.3.17)$$

While stress – optical coefficient related with the material's Young modulus as:

$$K \equiv K'\frac{1+v}{2E} \qquad (2.3.18)$$

3. Experimental

3.1. WGM excitation experimental setup

The experimental setup used for whispering gallery mode resonation within a polypropylene cylindrical microresonator is depicted in Fig. 7. Light from a CW infrared laser source (SLD) is transmitted through a single – mode optical fiber (SMF – 28) which is coupled with a 2.2μm diameter optical fiber taper. The taper, is used for whispering gallery mode (WGM) excitation within the polypropylene cylindrical cavity. After light interacting with the polypropylene cavity, is transmitted through the OFT to a polarizing optical fiber resolving into TE and TM modes. The signal obtained is guided through the same fiber, using an optical spectrum analyzer (OSA) (ANDO AQ6317B®).

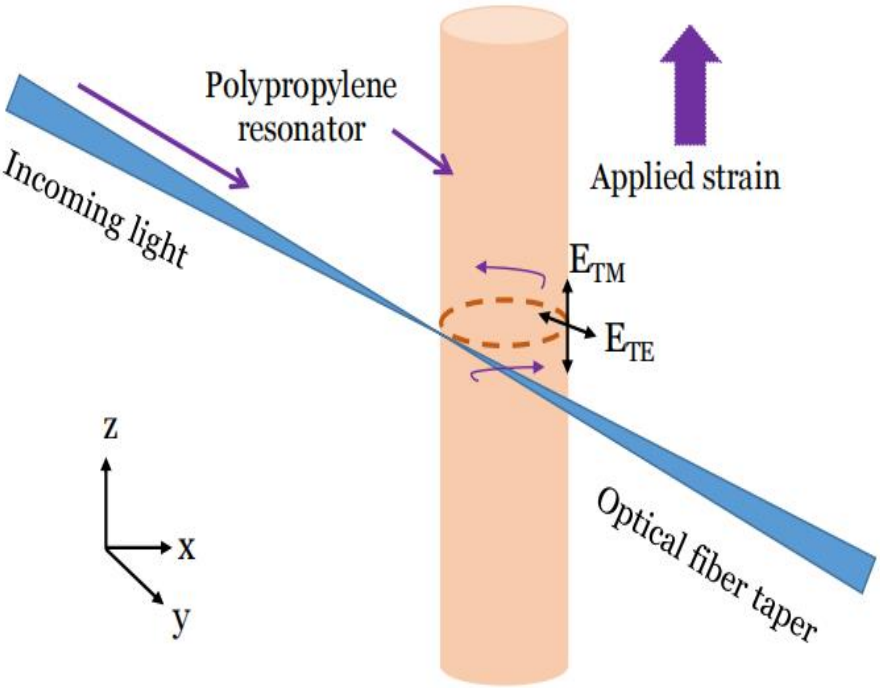

Figure 7: Experimental apparatus for polypropylene suture spectral characterization

For imaging light coupling between the PP cylindrical microcavity and the taper, we used a broadband lamp combined with a CMOS sensor –based camera with a 20x magnification objective lens.
The polypropylene microcavity is fixed on a specialty bronze mount, with fine thread Vernier adjustments. On top of this mount, a mechanical actuator (Z906® stage) is placed, applying controllable strain on the cylindrical resonator. The actuator is designed to perform 0.2 μm steps and is manipulated through a DC servo motor (TDC 001 cube). This system is also controlled automatically, through Kinesis® software, provided by Thorlabs®.
Signal is obtained using an optical spectrum analyzer.

3.1.2. Polypropylene no – core waveguide cavity

Polypropylene (PP) is a linear hydrocarbon polymer, expressed as $(C_3H_6)_n$. Polypropylene is a semi-rigid, cost-effective, and tough thermoplastic linear hydrocarbon polymer resin that offers excellent chemical, electrical, and fatigue resistance at high temperatures. It is considered a hazard-free plastic and as such, it is used for the production of products ranging from plastic furniture and machinery to pill containers and syringes. Depending the position of the methyl pendant group, PP can form three basic chain structures, atactic, isotactic and syndiotactic. Figure 8 below, illustrates these chain structures.

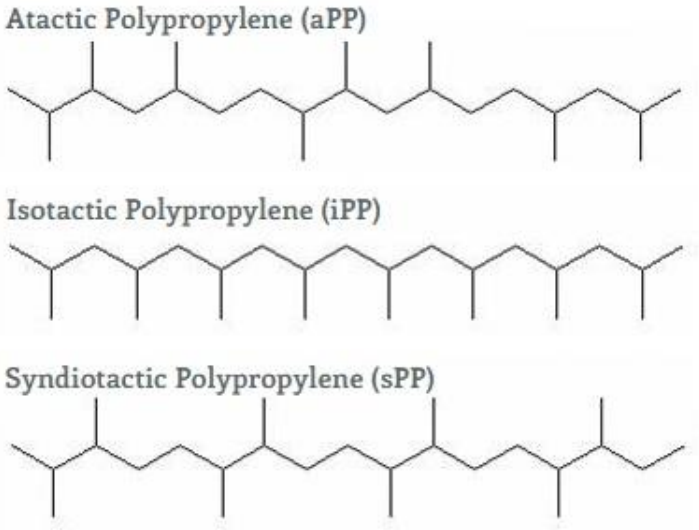

Figure 8: Polypropylene chain structures

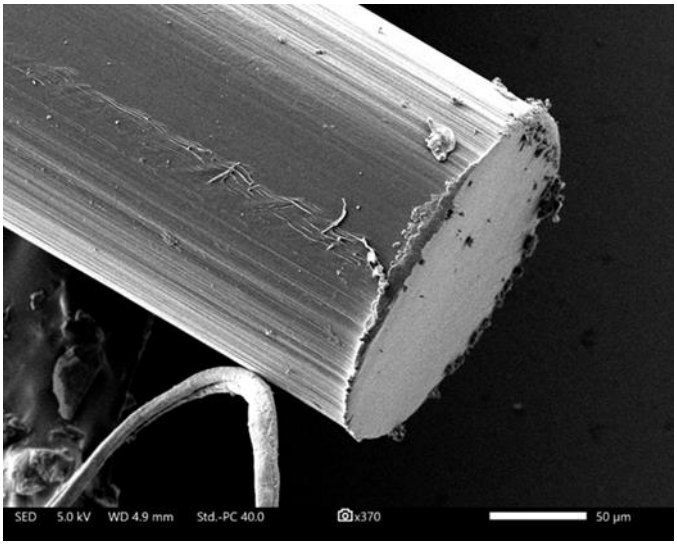

Figure 9: SEM image of the polypropylene microcavity

In WGM excitation experiments, polypropylene no – core waveguide cavities are used of cylindrical diameter, and diameter 150μm. They consist of polypropylene in its isotactic form, where all the methyl groups lay on the same side of the polymer chain, providing high crystallinity on the material.

3.2. Experimental Apparatus Calibration

3.2.1. Polarizing optical fiber calibration

A polarization maintaining fiber is a part of the experimental setup, in order to distinguish TE and TM polarization states, leading to the specific readout of the corresponding modes. A polarization maintaining optical fiber is made of a birefringent material, for maintaining the polarization state of the incoming light during propagation [44]. In our setup, the polarization maintaining optical fiber is placed on a rotating mount, indicating the rotation angle values, as shown in Figure 9. The fiber allows the propagation of a specific polarization state (TE or TM) when placed on the right angle. It is therefore crucial to determine the proper fiber angle leading to the excitation of TE or TM modes within the microcavity.

The fiber calibration setup is depicted in Figure 8. Light from a non – polarized tunable laser in the IR spectrum range (~1550 nm) is transmitted through a single mode fiber (SMF – 28) connected with the light source, and is collimated with the aid of two 10x objective lenses into the polarization maintaining fiber. A Rochon polarizer is also placed between the two lenses for selecting the polarization state. This polarizer, made with MgF_2 crystal, is used in order to distinguish the ordinary and extra – ordinary rays of the non – polarized incoming light when rotated at the right angle. The polarization maintaining fiber is then connected with an optical spectrum analyzer to obtain the transmitted signal. In order to perform the fiber's calibration, we rotate its mount by 10 degrees each time and obtain intensity measurements as a function of the fiber's angle. The obtained measurements are plotted in Figure 11, for the two different light rays exerting Rochon (ordinary and extra – ordinary ray).

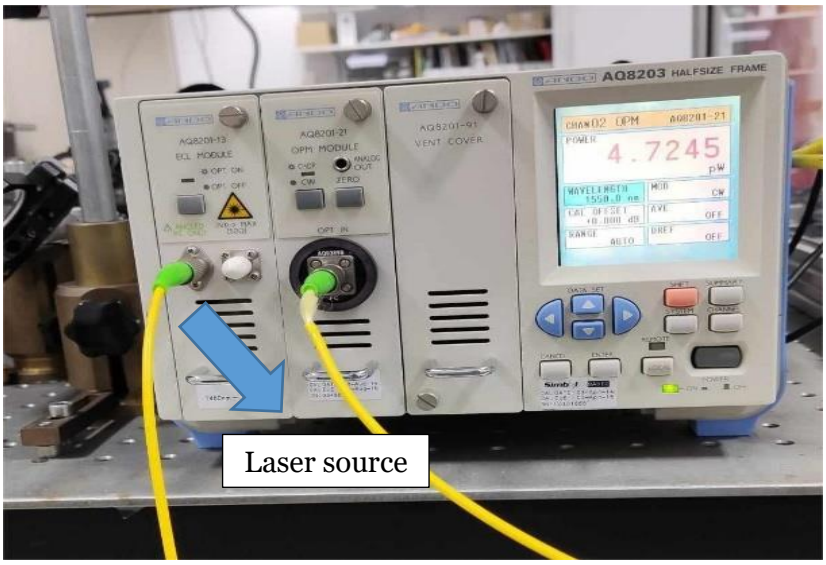

Figure 10 (a): Laser source – polarizing fiber calibration setup

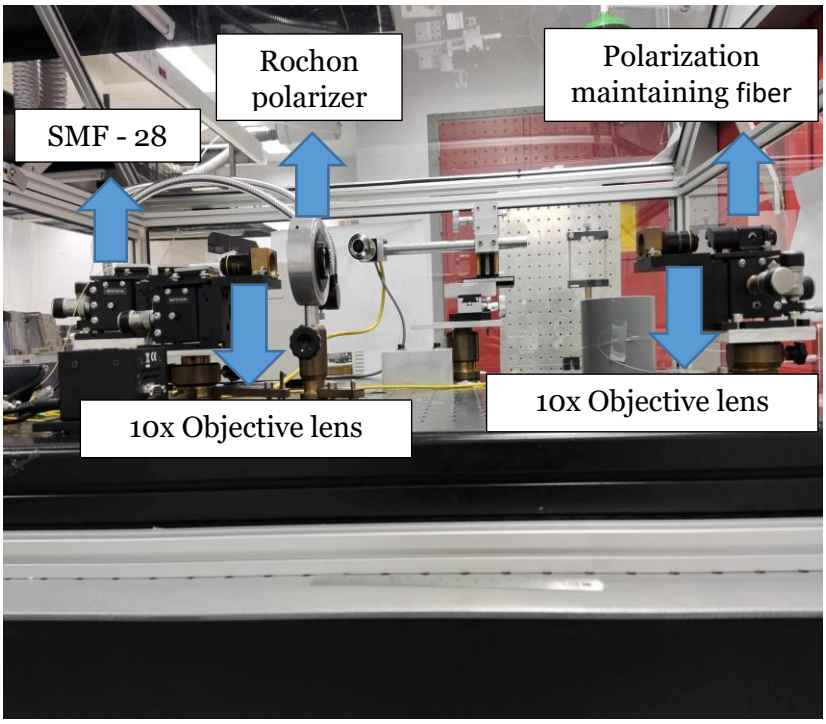

Figure 10 (b): Polarization maintaining fiber calibration setup

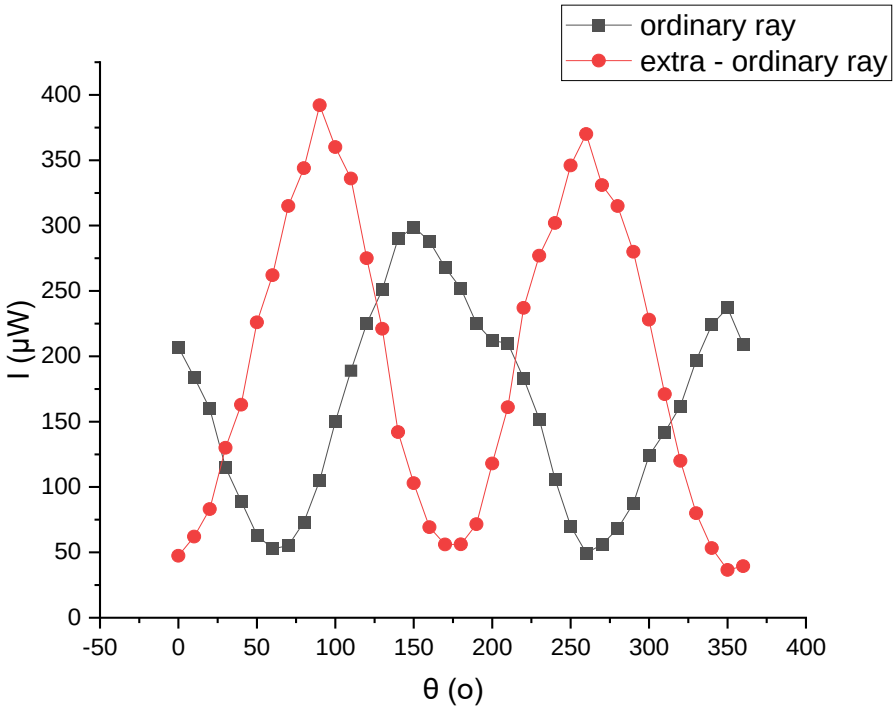

Figure 11: Intensity measurements vs polarizing fiber angle

From the measurements obtained, minima and maxima in intensity are observed for different angles. Using the above diagram and reference WGM spectra in SMF-28 optical fiber, using a former calibrated polarization maintaining fiber, we conclude that TE modes appear at 170^{o} while TM modes at 260^{o}, having a 90^{o} difference with each other.

3.2.2. Strain mount apparatus calibration

The polypropylene microcavities investigated in our experiments, are fixed on a bronze mount using small screws, as shown in Figure 12. On top of this mount, the mechanical actuator (Z906 stage by Thorlabs®) moves vertically, applying strain on the bottom part of the mount. The main issue arising in this setup is on how to accurately calculate the strain applied on the polypropylene resonator. A calibration of this system is necessary for maintaining high experimental accuracy.

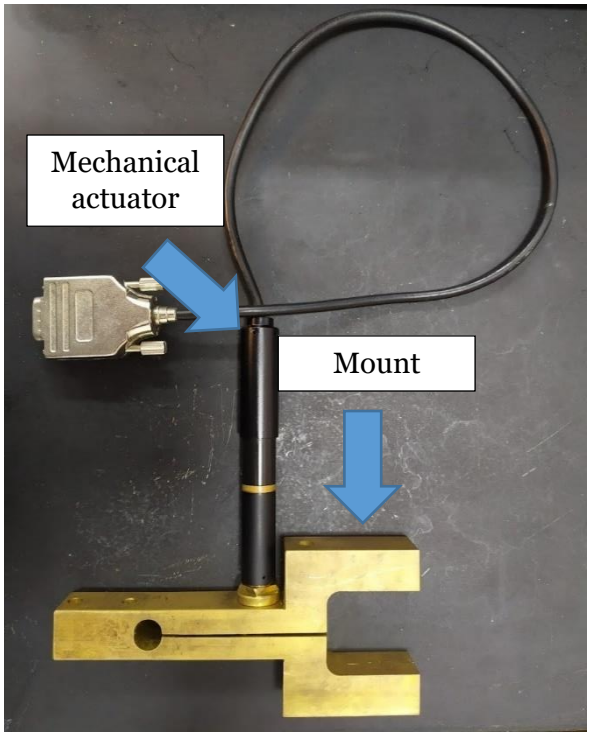

Figure 12: Resonator mount and mechanical actuator apparatus

Initially, we obtain strain measurements on an optical fiber Bragg grating (FBG) fixed with UV glue between two XYZ micrometric stages, in the way shown in Figure 13.

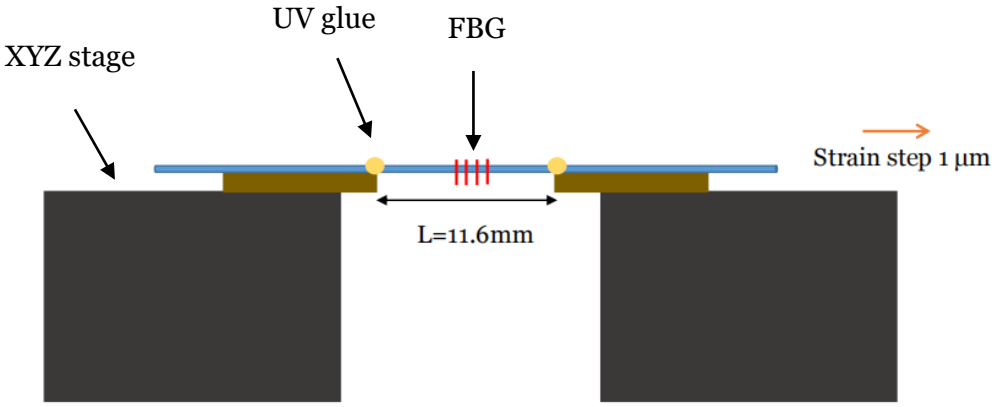

Figure 13: Experimental apparatus for determination of FBG's strain – optical coefficient

Knowing that the initial FBG's length is 11.6 mm, we can easily calculate the strain applied at each 1 μm micrometric stage displacement, using the form $\varepsilon = \frac{\Delta L}{L} = \frac{1\ \mu m}{11.6\times10^4 \mu m} = 8.6\ \mu\varepsilon$. As we apply strain on the grating, we obtain measurements of its transmission signal. From the spectral shifts observed, we can determine the FBG's strain – optical coefficient.

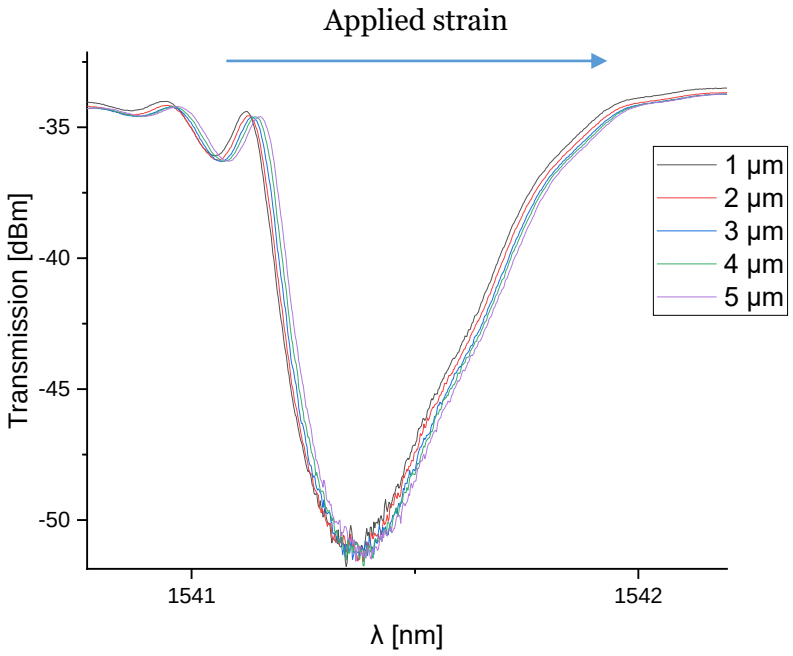

Figure 14: FBG transmission spectral shift vs applied strain

As shown in Figure 15 below, there is a linear response between the longitudinal strain applied and the Bragg wavelength of the FBG, The slope corresponds to the FBG's strain – optical coefficient and its value equals 0.92 pm/με, as shown in Figure 13 below.

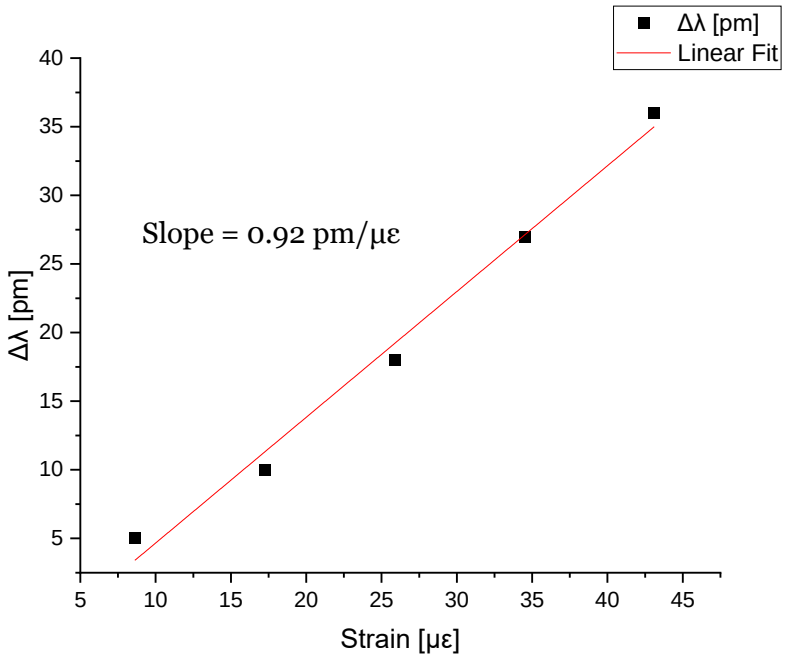

Figure 15: Spectral shift vs. applied strain measurements

The next step is to remove the grating from the stages and fix it on the metallic mount used in our experimental setup, using UV glue. As the actuator moves, applying strain on the mount, and therefore the microcavity, we also obtain the spectral shifts of the FBG transmission signal. Knowing the strain – optical coefficient of the grating, we can accurately calculate the strain applied on the mount at each actuator step. A figure of the actuator fork apparatus is depicted in Figure 16 (a), as well as the FBG's transmission spectra obtained for each step.

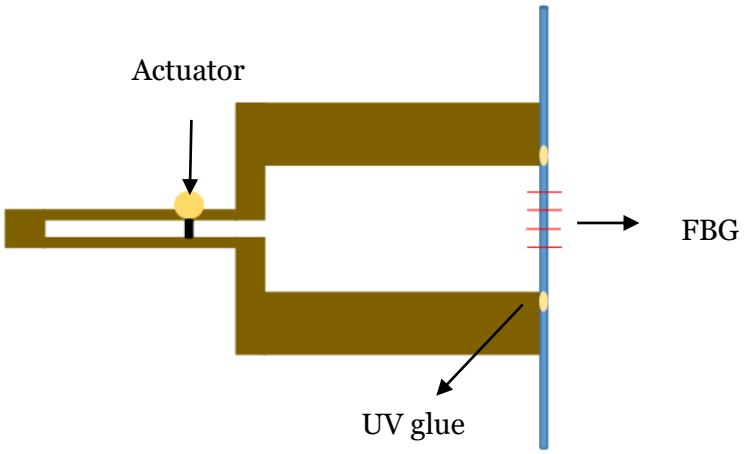

Figure 16 (a): Actuator mount apparatus

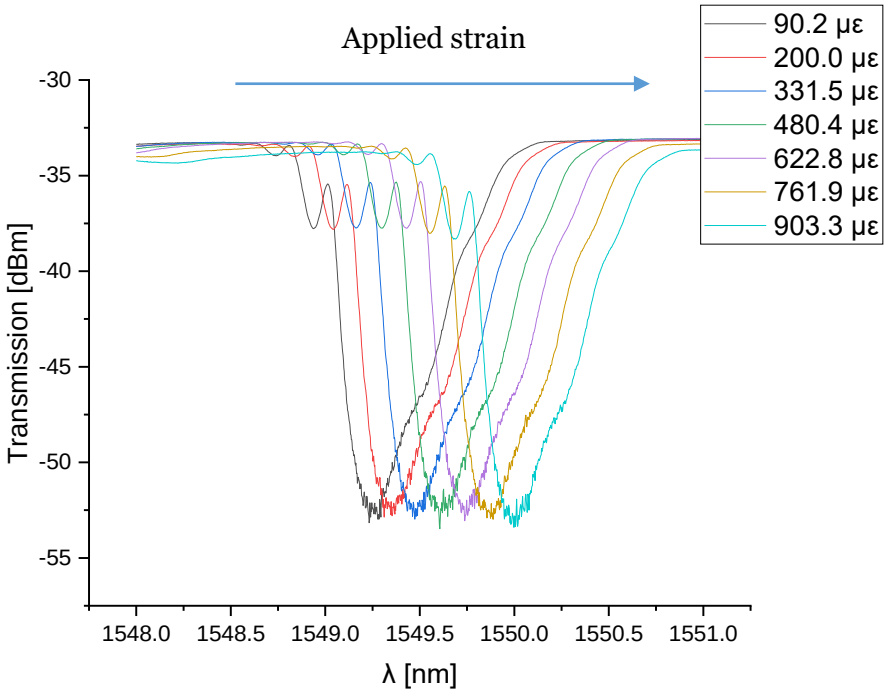

Figure 16 (b): FBG transmission signal shift for each strain step

The strains applied the polypropylene microcavities as a function of the actuator step, are plotted in the following diagram:

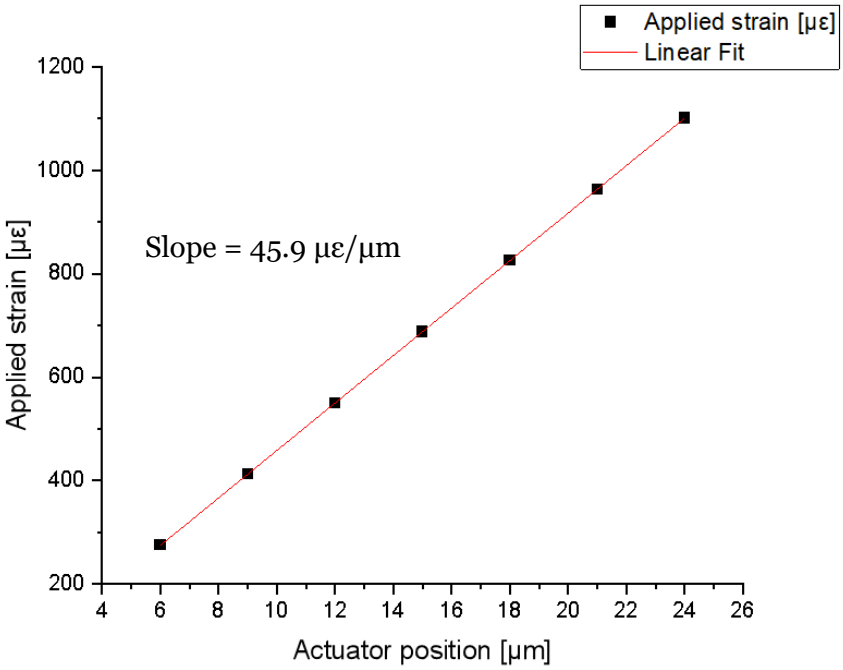

Figure 17: Applied strain vs. actuator position

A linear response of the applied strain as a function of the actuator position is observed from Figure 17. The slope related to this linear function corresponds to the amount of strain applied on the mount on each actuator step. The value of this slope indicates that the strain load is 45.9 με for each micrometer displacement step of the actuator.

4. Results and discussion

4.1. Simulation results

Light confinement in 150 μm diameter cylindrical polypropylene microcavities, is enhanced through multiple total internal reflections (TIRs) along the cylindrical surface, leading to the formation of distinct modes, supported within the resonator. During modal excitation using OFT a number of radial modes are excited leading to complex WGM spectrum that has to be identified and correlated with modal types (azimuthal and radial). Also, it is important to perform modal allocation for the identification of modes appearing in the obtained spectra. In order to examine the overall modal behavior, we perform simulations, using the finite element method (FEM) with the aid of COMSOL Multiphysics® computational program.

A careful design of the investigated problem is crucial for WGM characterization based on their radial (l) and azimuthal (m) orders. For this purpose, we assume a perfectly symmetric cylindrical geometry. A circular cross – sectional area made of polypropylene, with 150 μm diameter is selected as the resonant medium, which is surrounded by air, as shown in Figure 18. TE and TM modes formed within this cavity, correspond to the solutions of Maxwell's equations, combined with the appropriate boundary conditions on the interface between the two media, for the electric and magnetic field respectively. Figure 18 below, represents the investigated resonator, along with WGM formation in it. WGM resonances of 1st (l=1), 2nd (l=2) and 3rd (l=3) are shown.

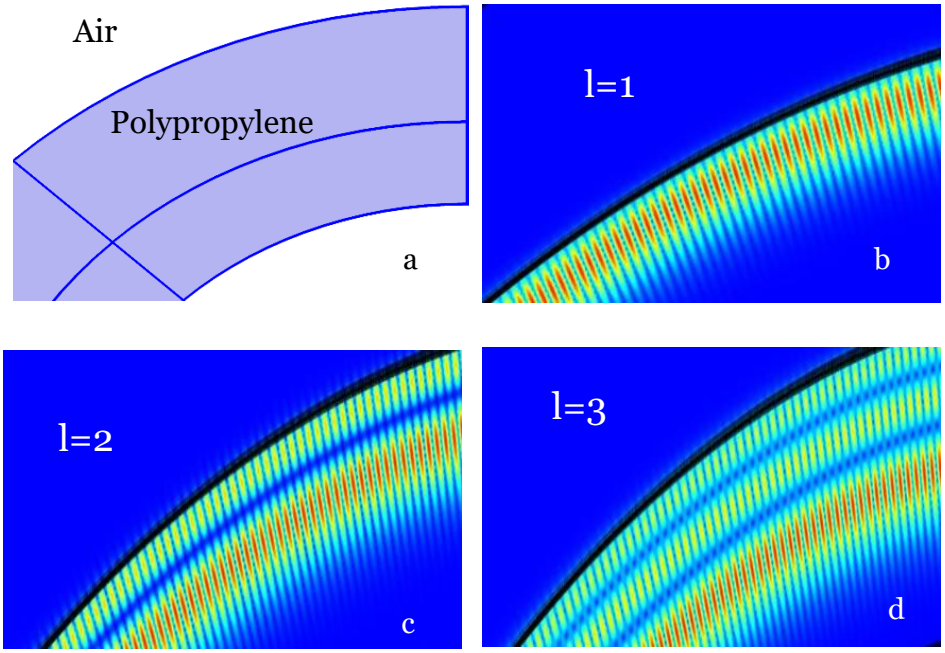

Figure 18: Schematic representation of the microresonator and WGM radial order modes

In order to perform modal allocation of the experimental WGM spectra obtained, eigenvalue simulations have been carried out. A part of the 2D cavity representation, is depicted in Figure 16 (a). In the cavity examined, homogeneity along the z – axis is assumed (d/dz=0). At first, we define the dimensional parameters related to this problem. Specifically, r_{cavity} = 75 μm and r_{air} = 80 μm are the radius values for the polypropylene cavity and surrounding air respectively. It should be mentioned that the cavity under study is assumed to have no external cladding. The refractive indices of these media are taken to be n_{cavity} = 1.4811 and n_{air} = 1.

Whispering Gallery Modes of first (l=1), second (l=2) and third (l=3) radial orders are observed in our experimental data. These eigenvalue problem solutions are also depicted in Figure 16 (b)-(d).

4.2. Spectral experimental results

4.2.1. WGMs in SMF – 28 optical fiber resonators

Our research work focuses on the investigation of light localization within cylindrical microresonators, and especially those made from polypropylene. In order to better understand the way light is confined inside resonators with this symmetry, we studied at first, WGM resonance formation within SMF – 28 optical fibers, as a reference point. SMF – 28 optical fibers are made of silica glass, with refractive index of n = 1.445. They are cylindrically symmetric, with radius r = 125 μm.

In our experiments, we obtained WGM spectra, formed within SMF – 28 fibers, using the same setup as the one described in Section 3.1, for both TE and TM polarization states. In these spectra, the resonances appear as notches, resulting from intensity drops for the resonant wavelengths. Using finite element method, we performed the modal allocation, with the aid of COMSOL Multiphysics® simulation program, similarly described as in the previous section, but changing the radius and refractive index to the values mentioned in this section. The WGM spectra obtained for TE and TM polarization states are presented in Figure 19 below.

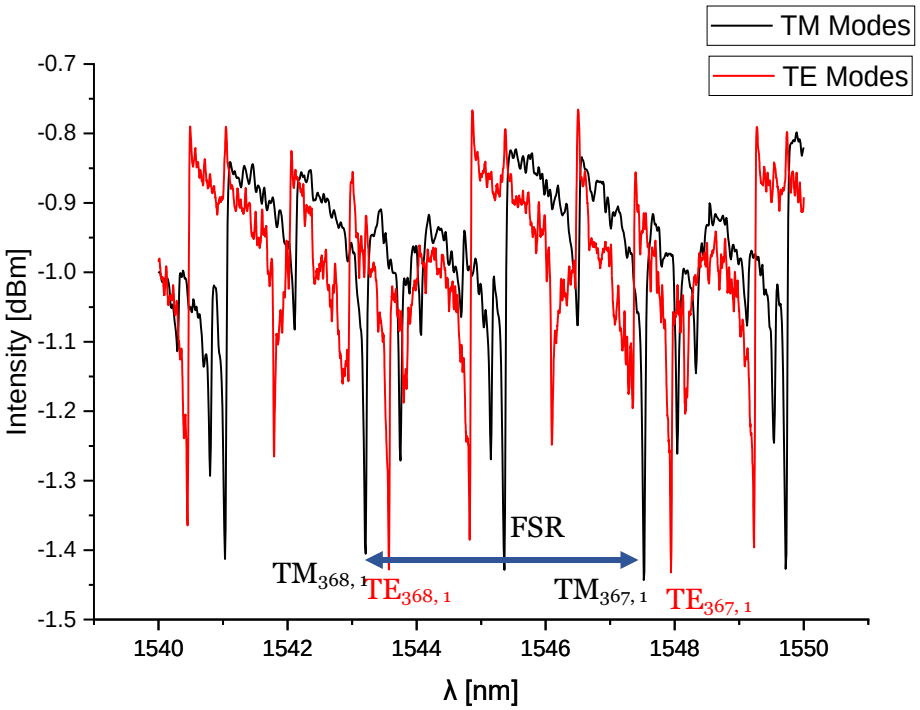

Figure 19: TE and TM WGMs on SMF – 28 optical fiber resonator

In Table 4.1, we present a comparison between the resonant wavelengths observed experimentally and the ones evaluated from the simulations.

Table 4.1: Experimental vs. simulation data of specific WGMs in SMF – 28 optical fiber

	Experimental data		**Simulation data**	
	TE Modes	TM Modes	TE Modes	TM Modes
l = 1	1543.6nm	1543.2nm	1543.0nm	1542.8nm
l = 1	1547.5nm	1547.9nm	1547.1nm	1547.6nm

The WGM spectra obtained, are related to two important parameters: the free spectral range (FSR) and Q factor, also related with the resonator's geometrical characteristics. FSR describes the frequency or wavelength spacing between two successive resonance peaks. FSR is related to the resonator radius through the following relationship:

$$FSR = \frac{\lambda_0^2}{2\pi nr} \qquad (4.1.1)$$

Where, λ_o is the resonant wavelength, n is the medium's refractive index, while r is the resonator radius.

Q factor is a dimensionless quantity, characterizing the resonance sharpness and providing a measure of energy storage within an optical system. Q factor can be defined as the ratio between the resonant wavelength over the FWHM of the resonant peak:

$$Q = \frac{\lambda_0}{FWHM} \qquad (4.1.2)$$

Therefore, the quality of the SMF – 28 spectra obtained, is strictly related to the above two parameters. Specifically, the FSR calculated from the obtained spectra equals to FSR = 4.3 nm, resulting in a fiber diameter of 2r = 123 μm. We also estimate the Q factors related to these resonances by fitting a spectral peak with a Lorentzian function. SMF – 28 resonant peaks appear to have Q factors of ~ 2×10^4.

Table 4.2: FSR and diameter calculations on SMF – 28 optical fiber

	FSR (nm)	**Diameter (Experimental) (μm)**	**Diameter (SMF – 28) (μm)**
TE Modes	4.35	122.0	125.0
TM Modes	4.31	123.0	125.0

4.2.2. WGMs in polypropylene microcavities

The main target of our work is the investigation of polypropylene's photo – elastic properties. For this purpose, in our experiments, we extensively investigate WGM formation inside cylindrical polypropylene microcavities. Furthermore, we examine the WGM spectral response to an applied strain. The modal shift observed while strain is applied on the resonator, correlates the optical and mechanical properties of the resonator material. In our work, we obtain the spectra mentioned for TE and TM polarization states and observe their behavior when the resonator undergoes mechanical deformation. In addition, we perform modal allocation as is described in section 4.1 of this chapter. Figure 20, depicts the spectral data obtained for (a) TE polarization and (b) TM polarization state over a broad wavelength range in the IR part of the spectrum, for the polypropylene resonator under study.

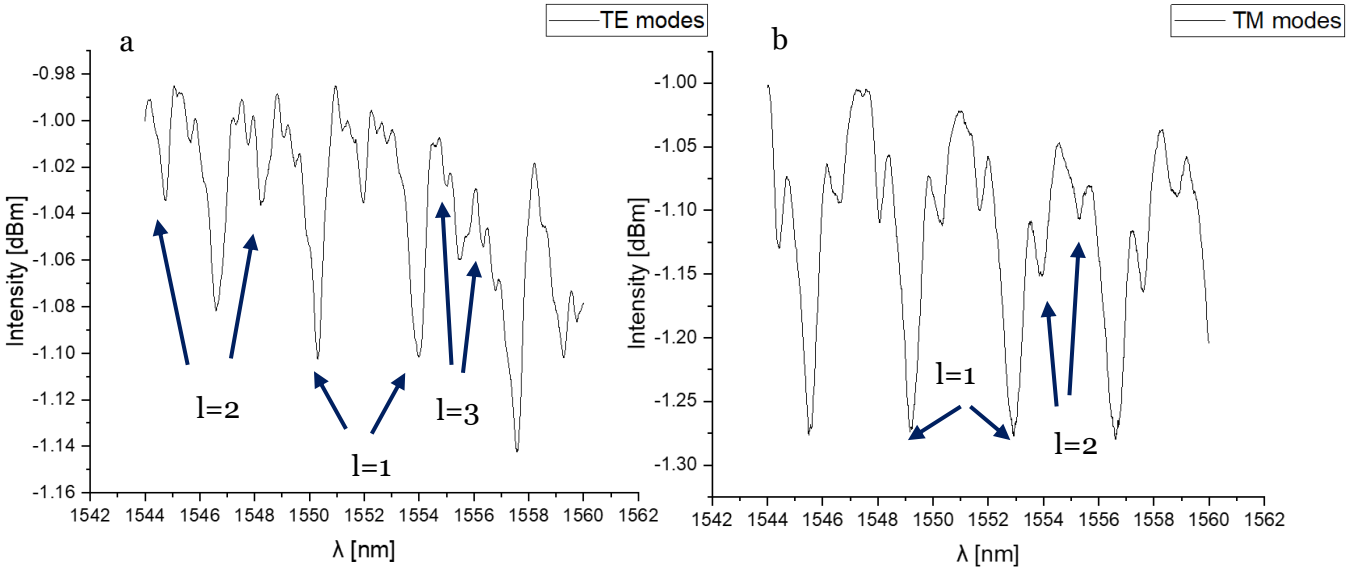

Figure 20: WGM resonance spectra for TE and TM polarization states indicating the modal orders observed

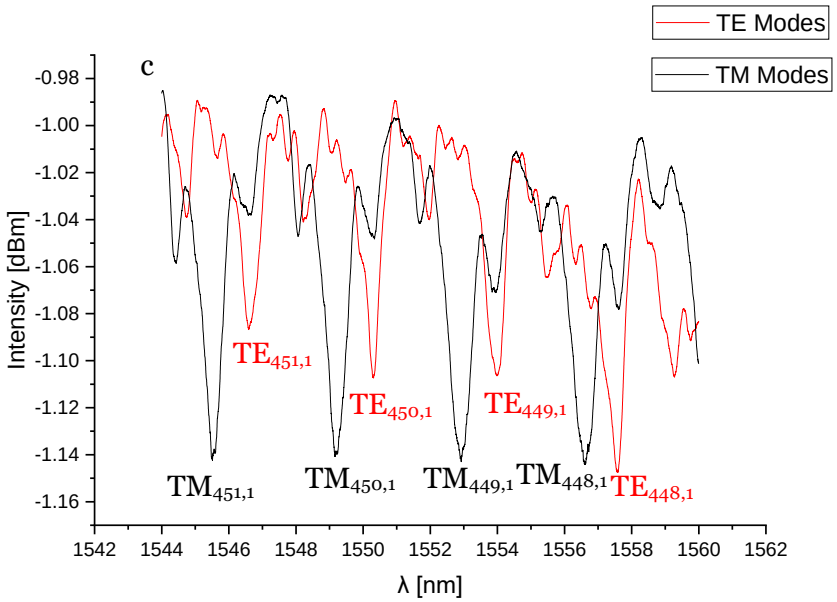

Figure 21: (a) TE WGMs (b) TM WGMs in polypropylene resonator (c) TE and TM WGMs merged in a single graph

In the spectra shown above, we observe WGM resonances of first (l=1), second (l=2) and third (l=3) orders for TE polarization, as indicated in the figure, while only resonances of first and second order are observed for TM polarization state. Table 4.3 summarizes a comparison between the spectral resonant wavelengths formed in polypropylene and the ones estimated from our simulations for first (l=1) and second (l=2) radial order WGMs.

Table 4.3: Experimental vs. simulation data of specific WGMs in polypropylene resonator

	Experimental data		**Simulation data**	
	TE Modes	TM Modes	TE Modes	TM Modes
l = 1	1550.3nm	1552.9nm	1550.4nm	1552.8nm
l = 2	1548.3nm	1548.2	1548.8nm	1548.8nm

These spectra provide information about the resonator size and resonance quality, through the FSR and Q factor, described in equations (4.1) and (4.2). Since we consider WGM resonances to be described by Lorentzian functions, after performing a proper fitting on $TM_{450,1}$ resonance peak the quality factor is found to be $Q \sim 1.7 \times 10^3$, since it is the highest in the cavity examined. The

resonant quality factor is approximately 10 times less in polypropylene than in SMF – 28 resonances. The free spectral range (FSR) is measured to be 3.60 nm in the TE modal spectrum and 3.50 nm in the TM modal spectrum. Free spectral range calculations for the polypropylene microresonator are gathered in Table 4.4.

Table 4.4: FSR calculations in polypropylene microcavity

	FSR (nm)	Diameter (Experimental) (μm)	Nominal diameter (Polypropylene resonator) (μm)
TE Modes	3.60	143.4	150.0
TM Modes	3.50	147.5	150.0

4.2.3. Polypropylene strain test results

The polypropylene microcavity is considered to be perfectly cylindrical ($\frac{\partial}{\partial z} = 0$). In COMSOL resonant simulations, it is estimated to be a circular 2D structure, as described in Section 4.1. The resonator undergoes mechanical deformation, as it is subjected to controllable strain along the z – axis. As polypropylene is elongated, changes in the arrangement and structure of its polymer chains are observed, influencing its optical refractivity and thus, refractive index and birefringence. These optically driven changes are also reflected in WGM resonance spectra.

As strain is applied on the resonator, a shift of WGM resonance peaks is observed. Figure 18, presents the transmission spectral shift of (a) $TE_{450,1}$ and (b) $TM_{450,1}$ resonances respectively. We observe that the resonant wavelength shift is oriented to the blue side of the spectrum. The calibration of the fork apparatus described in section 3.2.1, indicates that for each actuator step, the

applied strain is 45.9 με. In this case, the actuator is adjusted to perform a displacement of 10 μm at each step, applying 459 με strain on the mount. At each step, an averaged wavelength shift 0.5 nm is observed.

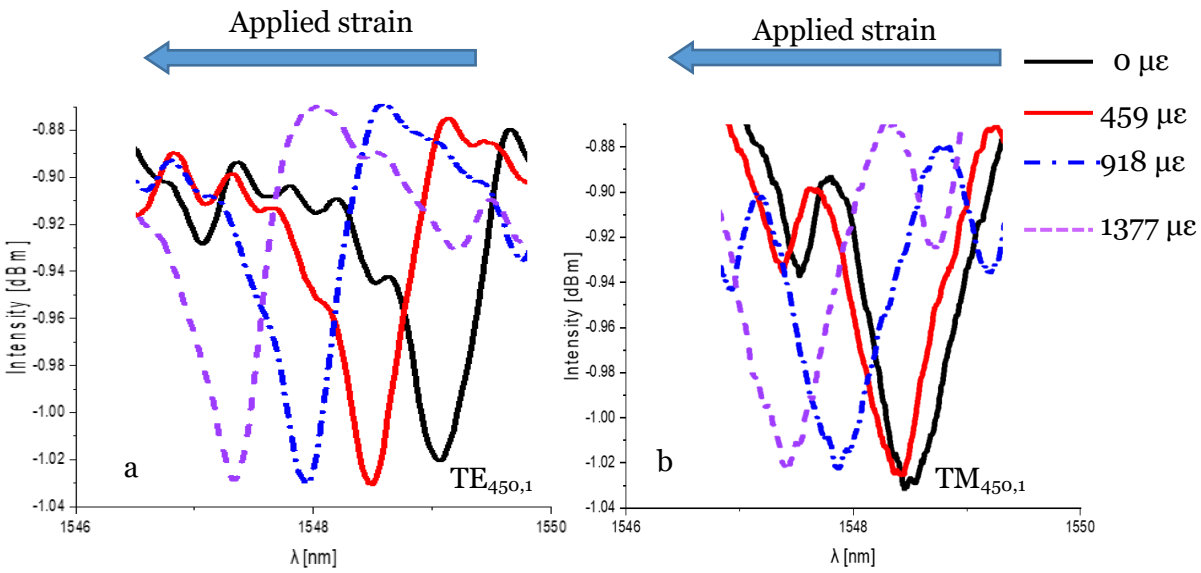

Figure 22: Transmission spectral shift of (a) $TE_{450,1}$ and (b) $TM_{450,1}$ resonance peaks under applied strain

Figure 22 illustrates the spectral shifts observed for TE and TM whispering gallery modes of the polypropylene resonator. The strain applied on the resonator causes a reduction of its radius, resulting in changes of the material's refractive index. This strain – induced birefringence is correlated to the wavelength shifts observed, through equation (2.3.16) presented in Chapter 2, written here again as:

$$\frac{\Delta n_{strain}}{n_0} = \frac{\Delta n_{TM}}{n_0} - \frac{\Delta n_{TE}}{n_0} = \frac{\Delta \lambda_{TM}}{\lambda_{TM}} - \frac{\Delta \lambda_{TE}}{\lambda_{TE}} \qquad (4.2.1)$$

The strain – induced birefringence increases linearly as a function of the applied strain. This linear behavior comes in agreement with previous studies in other cylindrical microresonators. Birefringence measurements vs axial applied strain are presented in Figure 23 below.

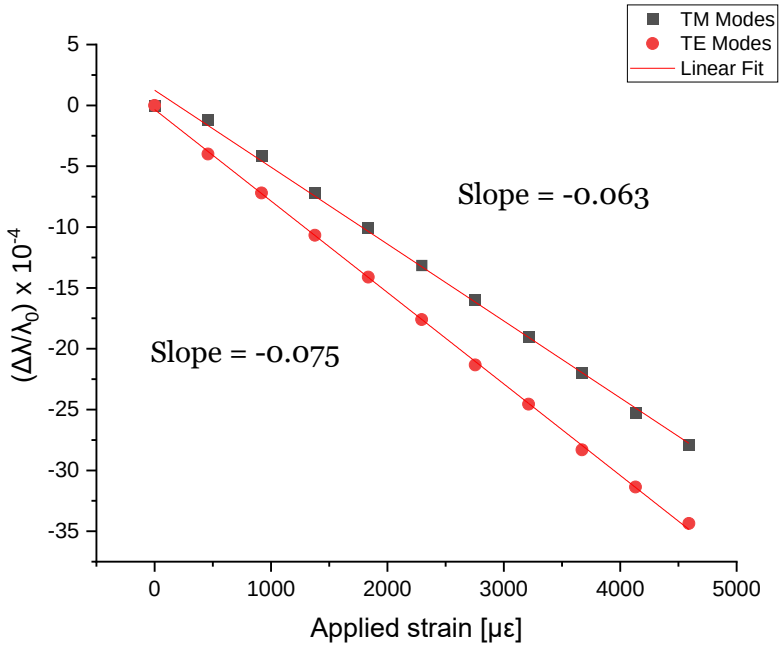

Figure 23: WGM spectral shift data vs applied strain for TE and TM polarization states

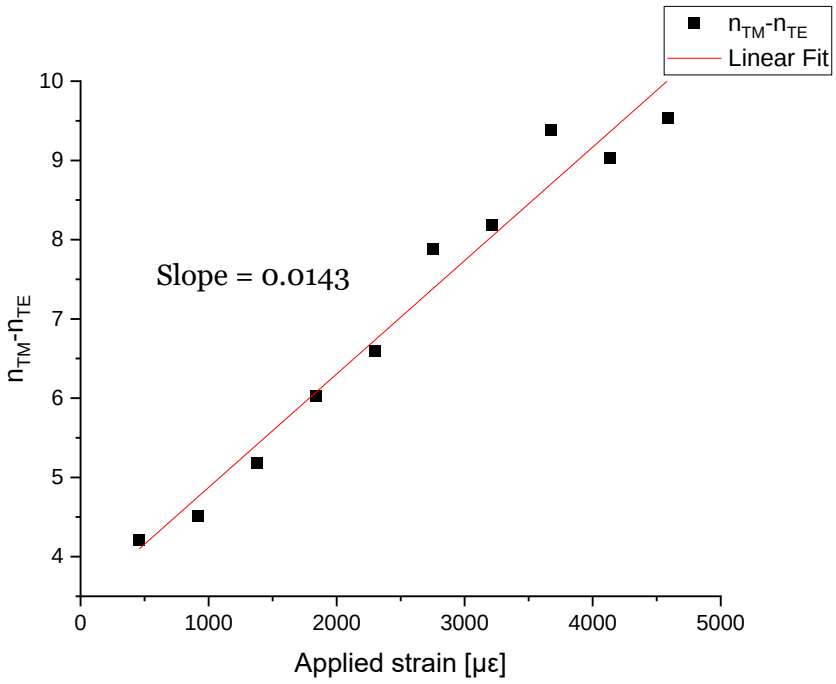

Figure 24: Strain – induced birefringence as a function of the applied strain

WGM spectral shifts indicate a linear behavior as a function of the applied strain, indicating no material detachment. Also, after relaxing the strains to the

initial state minor hysteresis (~0.3nm for TE and ~ 0.2nm for TM), indicating slowly elastic and minor plastic rearrangements into the polypropylene matrix. The slopes of wavelength shifts, however are not the same for TE and TM polarizations, although they fall in the same order of magnitude. Specifically, TE mode relative shift has a slope equal to -0.075, while the corresponding slope for TM mode resonances is -0.063, with a ~ 16% percentage difference between them. This difference probably indicate a degree of orientation of the polymer olefin chains, causing birefringence as the material undergoes elongation.

The wavelength slopes of Figure 19 are correlated with polypropylene's Pockel's coefficients p_{11} and p_{12} described in the strain – optical sensor of equation (2.3.3). Equations (2.3.8) and (2.3.9) form a 2 x 2 linear system, used for evaluating the coefficients mentioned. Equation (2.3.15) relates the observed slopes for each polarization, with a correction factor $C_{TE,\,TM}$, which is a small correction constant accounting for the intrinsic polarization sensitivity of TE and TM modes. The value of this constant is determined experimentally from measurements of the radius shrinkage (obtained by FSR values), and from the experimental values of the slopes mentioned. From our experimental results, we have to take into account a 0.01 correction factor. The photo – elastic properties of isotactic polypropylene, related with strain - and stress – optical coefficients, described in equations (2.3.17) and (2.3.18) respectively, are summarized in Table 4.5 below.

Table 4.5: Experimentally obtained photo – elastic properties of polypropylene microcavities

Photoelastic coefficients		**Strain – optical coefficient (K')**	**Stress – optical coefficient (K)**
p_{11}	p_{12}		
0.321758	0.313975	1.26×10^{-2}	6.88 Br

In order to calculate the parameters mentioned in Table 4.5, we considered the Young's modulus of isotactic polypropylene to be 1.3 GPa and the Poisson's

ratio to equal 0.42. Similar experiments have been carried out for the investigation of the photo – elastic properties in other polymers. For instance, in PMMA, the Pockels coefficients are: p_{11} = 0.298 and p_{12} = 0.294. PMMA is a well – known optical material. Therefore, a similarity in strain – optical coefficient behavior of the two polymers is observed. Of course, more experiments for the estimation of polypropylene's photo – elastic properties should be carried out for obtaining accurate results.

5. Conclusions

The purpose of our work was the investigation of the photo – elasticity of polypropylene polymer by employing whispering gallery mode resonation in cylindrical microcavities. Such a type of investigation is expected to be significant for the field of polymer science and soft photonic components, also for developing new types of optical sensors while exploiting the interesting chemical and mechanical properties of polypropylene.

In the studies performed in this thesis, isotactic polypropylene microcavities of approximate diameter of 150μm, were characterized by means of their whispering gallery mode light localization properties at the 1550nm band, while using optical fiber taper light excitation. Resulting Q – factors for those cavities obtained were ~ 1.7×10^3, together with FSR of ~ 147.5μm for the first order l = 1 radial modes. Additional investigations, included the theoretical simulation of those polypropylene microcavities using COMSOL for identifying modal order and confinement for the WGMs measured in these experiments.

Subsequently, these polypropylene WGM cavities were longitudinally strained using a motorized control unit and a specialty clamping fork, while obtaining spectra for TE and TM polarization, for different azimuthal modal states. The strain application resulted in blue shift of the corresponding WGMs of the same order, showing differential behavior for TE and TM polarization, manifesting strain induced birefringence of the order of 10^{-3} for typical strain of 5000 με.

From the above optical characterization measurements a strain optical coefficient of 1.26×10^{-2} was estimated for polypropylene, and Pockel's coefficients $p_{11} = 0.3218$ and $p_{12} = 0.3140$. Accounting the Young's modulus and Poisson's ratio of polypropylene, the stress – optical coefficient was estimated to be 6.88 Br.

We believe that the investigations carried out in this thesis will be a first step for implementation of polypropylene fibers and slabs in optical sensing applications, especially those subjected in continuous mechanical stimulations such those of wearables.

6. References

1. Velázquez-Ibarra, L., & Barranco, J. (2024). Resonant wavelengths of whispering gallery modes with a variable refractive index. *arXiv preprint arXiv:2403.00589*.
2. Matsko, A. B., & Ilchenko, V. S. (2006). Optical resonators with whispering-gallery modes-part I: basics. *IEEE Journal of selected topics in quantum electronics*, *12*(1), 3-14.
3. Armani, D. K., Kippenberg, T. J., Spillane, S. M., & Vahala, K. J. (2003). Ultra-high-Q toroid microcavity on a chip. *Nature*, *421*(6926), 925-928.
4. Yang, S., Wang, Y., & Sun, H. (2015). Advances and prospects for whispering gallery mode microcavities. *Advanced Optical Materials*, *3*(9), 1136-1162.
5. Ilchenko, V. S., & Matsko, A. B. (2006). Optical resonators with whispering-gallery modes-part II: applications. *IEEE Journal of selected topics in quantum electronics*, *12*(1), 15-32.
6. Chiasera, A., Dumeige, Y., Feron, P., Ferrari, M., Jestin, Y., Nunzi Conti, G., ... & Righini, G. C. (2010). Spherical whispering-gallery-mode microresonators. *Laser & Photonics Reviews*, *4*(3), 457-482.
7. Jiang, X., Qavi, A. J., Huang, S. H., & Yang, L. (2020). Whispering-gallery sensors. *Matter*, *3*(2), 371-392.
8. Kajfez, D. (2005). Q-Factor. *Encyclopedia of RF and Microwave Engineering*.
9. Riesen, N., Reynolds, T., François, A., Henderson, M. R., & Monro, T. M. (2015). Q-factor limits for far-field detection of whispering gallery modes in active microspheres. *Optics express*, *23*(22), 28896-28904.
10. Yi, T., & Kim, C. J. (1999). Measurement of mechanical properties for MEMS materials. *Measurement Science and Technology*, *10*(8), 706.
11. Milenko, K., Pissadakis, S., Gkantzounis, G., Aluculesei, A., & Fytas, G. (2017). Probing stress-induced optical birefringence of glassy polymers by whispering gallery modes light localization. *Acs Omega*, *2*(12), 9127-9135.
12. Melissinaki, V., Tsilipakos, O., Kafesaki, M., Farsari, M., & Pissadakis, S. (2021). Micro-ring resonator devices prototyped on optical fiber tapers by multi-photon lithography. *IEEE Journal of Selected Topics in Quantum Electronics*, *27*(6), 1-7.
13. Byrne, M., & Aly, A. (2019). The surgical suture. *Aesthetic surgery journal*, *39*(Supplement_2), S67-S72.
14. Korakas, N., Vurro, D., Tsilipakos, O., Vasileiadis, T., Graczykowski, B., Cucinotta, A.,... & Pissadakis, S. (2023). Photo-elasticity of silk fibroin harnessing whispering gallery modes. *Scientific Reports*, *13*(1), 9750.
15. K. Okamoto, "Chapter 1 - Wave theory of optical waveguides," in *Fundamentals of Optical Waveguides (Second Edition)*, Second Edi., K. Okamoto, Ed. Burlington: Academic Press, 2006, pp. 1–12.

16. International Telecommunications Union, “Optical Fibres, Cables and Systems,” pp. 144–147, 2009.

17. Alhaider, “Chapter 3 – Characteristics of optical fibers” M. (2017). *Optical Fiber Communications*, 5th Edition, Notion Press.

18. E. Hecht, *Optics*. Pearson, 2012.

19. Y. Sun, S. I. Shopova, G. Frye-Mason, and X. Fan, “Rapid chemical-vapor sensing using optofluidic ring resonators,” *Opt. Lett.*, vol. 33, no. 8, pp. 788–790, Apr. 2008.

20. V. M. N. Passaro, F. Dell’Olio, and F. De Leonardis, “Ammonia Optical Sensing by Microring Resonators,” *Sensors*, vol. 7, no. 11, pp. 2741–2749, 2007.

21. Yariv, “Yariv A., Yeh P.-Photonics_ Optical Electronics in Modern Communications (2007).” .

22. D. Marcuse, “Theory of dielectric optical waveguides,” 1974.

23. T. Ioppolo, J. Stubblefield, and M. V Ötügen, “Electric field-induced deformation of polydimethylsiloxane polymers,” *J. Appl. Phys.*, vol. 112, no. 4, p. 44906, 2012.

24. R. Black and L. Gagnon, *Optical Waveguide Modes: Polarization, Coupling and Symmetry*. 2010.

25. S. W. Harun, K. S. Lim, C. K. Tio, K. Dimyati, and H. Ahmad, “Theoretical analysis and fabrication of tapered fiber,” *Optik (Stuttg).*, vol. 124, no. 6, pp. 538–543, 2013.

26. Chenari, Z., Latifi, H., Ghamari, S., Hashemi, R. S., & Doroodmand, F. (2016). Adiabatic tapered optical fiber fabrication in two step etching. *Optics & Laser Technology*, *76*, 91-95.

27. B. R. Johnson, “Theory of morphology-dependent resonances: shape resonances and width formulas,” *J. Opt. Soc. Am. A*, vol. 10, no. 2, pp. 343–352, 1993.

28. J. D. Love, “Evanescent wave coupling of whispering gallery modes of a dielectric cylinder,” *IEE Proc. J*, vol. 140, no. 3, pp. 177-188(11), 1993.

29. Hall, J. M., Afshar, V. S., Henderson, M. R., François, A., Reynolds, T., Riesen, N., & Monro, T. M. (2015). Method for predicting whispering gallery mode spectra of spherical microresonators. *Optics express*, *23*(8), 9924-9937.

30. M. L. Gorodetsky, A. A. Savchenkov, and V. S. Ilchenko, “Ultimate Q of optical microsphere resonators,” *Opt. Lett.*, vol. 21, no. 7, pp. 453–455, 1996.

31. V. B. Braginsky, M. L. Gorodetsky, and V. S. Ilchenko, “Quality-factor and nonlinear properties of optical whispering-gallery modes,” *Phys. Lett. A*, vol. 137, no. 7, pp. 393–397, 1989.

32. M. L. Gorodetsky, A. D. Pryamikov, and V. S. Ilchenko, “Rayleigh scattering in high-Q microspheres,” *J. Opt. Soc. Am. B*, vol. 17, no. 6, pp. 1051–1057, 2000.

33. Delgado-Pinar, M., Roselló-Mechó, X., Rivera-Pérez, E., Díez, A., Cruz, J. L., & Andrés, M. V. (2019). Whispering gallery modes for accurate characterization of optical fibers’ parameters. In *Applications of Optical Fibers for Sensing* (pp. 1-19). London, UK: IntechOpen.

34. J. R. Wait, “Electromagnetic Whispering Gallery Modes in a Dielectric Rod,” *Radio Sci.*, vol. 2, no. 9, pp. 1005–1017, 1967.

35. M. L. Gorodetsky and V. S. Ilchenko, “Optical microsphere resonators: optimal coupling to high-Q whispering-gallery modes,” *J. Opt. Soc. Am. B*, vol. 16, no. 1, pp. 147–154, Jan. 1999.

36. M. H. Sadd, Ed., “Appendix D - Review of Mechanics of Materials,” in *Elasticity (Second Edition)*, Second Edi., Boston: Academic Press, 2009, pp. 518–531.

37. Š. Višňovský, *Optics in Magnetic Multilayers and Nanostructures*. 2006.

38. X. Roselló-Mechó, M. Delgado-Pinar, A. Díez, and M. V Andrés, “Measurement of Pockels’ coefficients and demonstration of the anisotropy of the elasto-optic effect in optical fibers under axial strain,” *Opt. Lett.*, vol. 41, no. 13, pp. 2934–2937, Jul. 2016.

39. Duong Ta, V., Chen, R., Ma, L., Jun Ying, Y., & Dong Sun, H. (2013). Whispering gallery mode microlasers and refractive index sensing based on single polymer fiber. *Laser & Photonics Reviews*, *7*(1), 133-139.

40. Lemieux-Leduc, C., Guertin, R., Bianki, M. A., & Peter, Y. A. (2021). All-polymer whispering gallery mode resonators for gas sensing. *Optics express*, *29*(6), 8685-8697.

41. Righini, G. C., Dumeige, Y., Féron, P., Ferrari, M., Nunzi Conti, G., Ristic, D., & Soria, S. (2011). Whispering gallery mode microresonators: fundamentals and applications. *La Rivista del Nuovo Cimento*, *34*, 435-488.

42. Kavungal, V., Mallik, A. K., Farrell, G., Wu, Q., & Semenova, Y. (2017). Strain-induced spectral tuning of the whispering gallery modes in a cylindrical micro-resonator formed by a polymer optical fiber. *Applied Optics*, *56*(5), 1339-1345.

43. Kavungal, V., Farrell, G., Wu, Q., Mallik, A. K., & Semenova, Y. (2018). A packaged whispering gallery mode strain sensor based on a polymer-wire cylindrical micro resonator. *Journal of Lightwave Technology*, *36*(9), 1757-1765.

44. Kaminow, I. P. (1984). Polarization-maintaining fibers. *Applied Scientific Research*, *41*, 257-270.

45. Ramgopal Madugani, Yong Yang, Jonathan M Ward, John Daniel Riordan, Sara Coppola, Veronica Vespini, Simonetta Grilli, Andrea Finizio, Pietro Ferraro, and Síle Nic Chormaic, "Terahertz tuning of whispering gallery modes in a PDMS stand-alone, stretchable microsphere," Opt. Lett. 37, 4762-4764 (2012).

46. Wolf von Klitzing *et al* 2001 *New J. Phys.* **3** 14.

47. X. Roselló-Mechó, M. Delgado-Pinar, A. Díez, and M. V. Andrés, "Measurement of Pockels’ coefficients and demonstration of the anisotropy of the elasto-optic effect in optical fibers under axial strain," Opt. Lett. 41, 2934-2937 (2016).

48. X. Roselló-Mechó, M. Delgado-Pinar, A. Díez, and M. V. Andrés, "Measurement of the strain-optic coefficients of PMMA from 800 to 2000 nm," OSA Continuum 3, 441-446 (2020).

49. N. Kokkinidis, N. Korakas, and S. Pissadakis, "Estimation of photo-elastic coefficients in ion-exchanged borosilicate glass cavities through whispering gallery mode resonation," in *Conference on Lasers and Electro-Optics/Europe (CLEO/Europe 2023) and European Quantum Electronics Conference (EQEC 2023)*, Technical Digest Series (Optica Publishing Group, 2023), paper ce_p_7.

50. Inoue, T. (2021). Strain-induced birefringence of amorphous polymers and molecular design of optical polymers. *ACS Applied Polymer Materials*, *3*(5), 2264-2273.